Available online at www.sciencedirect.com
SCIENCE DIRECT®

ELSEVIER

Journal of Hydrology xx (2005) 1–30

Journal of Hydrology
www.elsevier.com/locate/jhydrol

Multifractals, cloud radiances and rain

S. Lovejoy[a,*], D. Schertzer[b]

[a]Physics, McGill University, 3600 University st., Montreal, Que., Canada
[b]Cereve, Ecole Nationale des Ponts et Chaussées, 6-8, avenue Blaise Pascal, Cité Descartes 77455, Marne-La-Vallee Cedex, France

Accepted 8 February 2005

Abstract

The extreme variability of rainfall over huge ranges of space–time scales makes direct rain gauge measurements of areal rainfall impossible; assumptions about the rainfall scaling—whether trivial (homogeneous), or multifractal (heterogeneous)—are required even for interpolation. The alternative is to use rain surrogates such as radar reflectivities or those based on visible-infra red radiances. In this paper, we argue that cloud radiances should be studied to obtain basic information about the range and type of scaling in the atmosphere. Since, rain and clouds are strongly non-linearly coupled—and since the scaling of the fields, the scale invariance of the generators/exponents is a symmetry principle—a break in the scaling in one of the fields would cause a break in the other. Using 909 images from three satellites and six sensors (visible and infra red) collectively spanning the range of scales 5000–1 km, we demonstrate that power law scaling is respected to within an error of ±0.3–0.5%; that an upper bound on the deviations from the theoretical universal multifractal scaling is 1–2% per octave in scale. We also show that the outer scale of the cascade is very close to 20,000 km, the largest great circle distance on the earth. Allowing for (one-parameter) subpower law (logarithmic) scaling corrections we show that universal multifractal cascades starting at this scale explain the isotropic moments (order ≤1.6) to within an error of ±0.8%. We argue that the scaling of these isotropic statistics shows that the diversity of cloud morphologies reflects differences in anisotropies which are effectively washed out by the isotropic statistical methods used. We compare and contrast existing multifractal models showing which can be used as realistic cloud and rain models. We go on to use continuous in scale, anisotropic, space–time multifractal rain and cloud simulations (including radiative transfer) to show how diverse cloud, rain and radiance morphologies can be compatible with the observed isotropic scaling statistics. Finally, we argue that these will be necessary for solving measurement problems including the use of rain gauge, radar and visible/infra red surrogate fields.

1. Introduction

To the human senses, rain is surely one of the most extremely variable of atmospheric fields: directly palpable temporal variability ranges from fractions of a second to generations. The simplest assumption about processes occurring over wide ranges of scale is that they are scaling; indeed in the past, hydrological problems directly motivated key scaling advances including long range dependency (notably the 'Hurst phenomenon' (Hurst, 1951)), 'simple scaling' (Mandelbrot and Van Ness, 1968) and more recently,

---

* Corresponding author. Tel.: +1 514 398 6537.
E-mail address: lovejoy@physics.mcgill.ca (S. Lovejoy).

0022-1694/$ - see front matter © 2005 Published by Elsevier B.V.
doi:10.1016/j.jhydrol.2005.02.042

multifractals (see below for references). In the last 15 years in the fields of hydrology and meteorology, there has been an explosion of interest in multifractals. This is perhaps not surprising since, going back to (Richardson, 1922) cascades have been hypothesized to be a dominant dynamic atmospheric process and cascade processes generically give rise to multifractals. More generally, cascades occur in systems with a large number of degrees of freedom, where the same basic dynamical mechanism operates over a wide range of scales (when it is scale invariant in some very general sense). The main additional requirements for cascades are that some flux is conserved from one scale to another, and that the interactions are mostly between structures at neighbouring scales.

In the turbulence community, there is now a fairly broad consensus that the dynamic velocity field is multifractal—at least over some significant range from the dissipation scale (millimeters) to an outer bound discussed below. For the velocity field, there is even a fairly wide consensus about the actual multiscaling structure function exponent $\xi(q)$ (see the review, Anselmet et al., 2001) at least for statistical moments q in the range 1–7 (Meneveau and Sreenivasan, 1987a; Schmitt et al., 1992, 1996; Ruiz Chavarria et al., 1995). Debate is now concentrated on the high order moments (do they diverge as expected for canonical multifractals, or are they finite?) and low order moments (is $\xi(q)$ nonanalytic at the origin as expected by universality arguments?).

At first sight the values of the consensus exponents appear small. For example, the value of C_1, the codimension of the singularity giving the dominant contribution to the mean velocity is only ≈ 0.07 (compared to 0 for an nonintermittent, space-filling classical process). If we consider the conserved energy flux (proportional to the cube of the velocity), then the corresponding exponent is 0.36, still not enormous. Over a range of $\lambda = 10^2$ in scale (typical of many conventional numerical models, e.g. GCM's), this implies that the corresponding fraction of space giving a significant contribution to the mean is $\lambda^{-C_1} = 100^{-0.36} \approx 19\%$ which shows that over 80% of the model grid elements will have fluxes too low to significantly contribute to the mean energy flux. Nevertheless, this may well be adequately modeled; it explains how such standard models can be 'adjusted' by judicious 'parametrisation' to give reasonable looking results over their narrow scale ranges. However, if this scaling behaviour is valid over the full range (planetary/dissipation range $\approx 10^4$ km/10^{-3} m $= 10^{10}$), then the corresponding fraction is only 0.02% (if we consider the variance of the flux, the exponent is 1.03 and the fraction is 5×10^{-11}). This quantitatively demonstrates the drastic effects of multifractal intermittency even when a relatively 'calm' multifractal process operates over a wide enough range of scales. Over small enough scale ranges conventional parametrisations may be workable; but these will not be valid outside of the relatively narrow range over which they were calibrated. We shall see that the same conclusions hold for clouds radiances—and by implication—rain, with the same consequences for standard point process type cluster models (e.g. Waymire and Gupta, 1981).

Since, rain is strongly coupled with the highly turbulent wind field, this turbulence consensus is in itself of fundamental significance to hydrology and explains the recent finding (Desaulniers-Soucy, 1999; Lilley et al., in press; Lovejoy et al., 2003) from the stereophotographic HYDROP experiment that rain is multifractal down to very small scales only becoming statistically homogeneous at scales less than a meter. Indeed, new analyses of this unique data set have recently directly linked classical turbulence and the rain liquid water density: the LWC density spectrum is very nearly $k^{-5/3}$, i.e. the same as that of a scalar passively advected by a turbulent wind only becoming white noise at scales of 50 cm or less (depending somewhat on meteorological conditions). The rain-rate—which depends not only on the LWC but also on the drop fall speed is thus an 'active' not passive turbulent scalar. The turbulent scales are thus a nonclassical multifractal *discontinuum* which has important implications not only for cloud physics but also for the measurement of rain.

What is the outer limit of scaling in rain? If we restrict our attention to direct measurements of rain, many studies over various ranges of space and/or time scale have been performed but without the emergence of a consensus: e.g. (Lovejoy, 1981, 1982; Bell, 1987; Lovejoy et al., 1987; Zawadzki, 1987; Seed, 1989; Lovejoy and Schertzer, 1990; Gupta and Waymire, 1990; Rosso and Burlando, 1990; Lovejoy and Schertzer, 1991; Fraedrich and Larnder, 1993; Hubert et al., 1993; Kumar and Foufoula-Georgiou, 1993; Ladoy et al., 1993; Gupta and Waymire, 1993; Olsson et al., 1993; Tessier et al., 1993; Larnder, 1995; Zawadski, 1995; Lovejoy and Schertzer, 1995b; Hubert et al., 1995; Olsson, 1995; Over and Gupta, 1996b; Fabry, 1996; Harris et al., 1996; Burlando and Rosso, 1996; Yano et al., 1996; Menabde et al., 1997; De Lima, 1998; De Lima et al., 2001). One reason for this lack of consensus is that all the measurement techniques—including the different varieties of rain gauge—have their own non-trivial 'observer' problems, see e.g. (Lovejoy et al., 1996). However, if we consider evidence from other data—notably satellite cloud radiances, then the measurement problem is much more straightforward. In addition, visible and infra red radiances are routinely used—either directly or indirectly—as rain surrogates in satellite rain algorithms so that results on radiances have direct implications for rainfall.

The cloud radiances are relevant since they are strongly non-linearly coupled to the rain and to the dynamics, and since scaling (scale invariance of the generators/exponents) is a dynamical symmetry. The scaling in the former is therefore an indication of scaling in the latter. In addition, since due to gravity the atmosphere is strongly stratified—at least over this critical range from meso to synoptic scales—this result effectively rules out the existence of *isotropic* turbulence regimes. Indeed, recent results from high powered lidar of passive scalars (Lilley, 2003; Lilley et al., 2004), and the discovery of the fractality of at least some aircraft trajectories (Lovejoy et al., 2004), has given substantial new and direct support for the unified scaling model (Schertzer and Lovejoy, 1985b; Lovejoy et al., 1993). This model involves the horizontal wind following a Bogliano–Obhukhov $k^{-11/5}$ scaling in the vertical and a Kolmogorov $k^{-5/3}$ spectrum in the horizontal; so that vertical sections of structures become progressively flatter at larger and larger scales in a power law way. Although such differential scaling was demonstrated in rain with radar data in (Lovejoy et al., 1987) it was over a range of scales of only 8 in the vertical.

These results suggest that if we generalize the notion of scale invariance to handle anisotropy which varies scale by scale in a scaling manner, then we can start to make sense of the wind spectra and other data. Going a step further, and generalizing to scaling position dependent anisotropy (nonlinear GSI), we can—at least in principle—reconcile the diversity of cloud types and morphologies with the scaling of the isotropic cloud statistics analyzed in (Lovejoy et al., 1993; Tessier et al., 1993).

In the following, we present results from the largest scaling of the atmosphere to date (involving 909 satellite images); we attempt to quantify the accuracy with which isotropic scaling statistics are valid and with the help of multifractal simulations to show how diverse cloud, rain and radiance morphologies are (at least in priniciple) compatible with the observations. In Section 2, we concentrate on a spectral analysis of cloud radiances from six sensors on three satellites spanning the range of scales 1–5000 km. In Section 3, we present an overview of multifractal properties, models and simulation techniques (including for anisotropic space–time rain modeling). Finally, we show that deviations from the theoretical multiscaling statistics are very small (Section 4). The primary data analysis is a partial summary of work presented in an MSc thesis (Stanway, 2000).

2. Satellite spectral evidence for wide range scaling

2.1. Discussion

Theoretically, the ideal would be to test the extent and type of rain scaling directly. However, precipitation is not easy to measure; in addition, due to the strong intermittency (variability) it is very difficult to get adequate statistics. Individual raingauges such as tipping buckets operate with a fixed depth of rain resolution so that their temporal resolution varies with the rain rate introducing spurious breaks in the scaling (De Lima, 1998). When used for estimating areal rainfall, account must be taken of the sparse fractal nature of typical networks (Lovejoy et al., 1986; Tessier et al., 1993, 1994), and non-standard multifractal objective techniques should be used (Salvadori et al., 2001). Radar data measure the volume averaged effective radar reflectivity and has a range dependent resolution which affects the statistics.

Cloud radiances, on the other hand have many advantages. For example, a single cloud scene 1000 pixels on a side has an information content comparable to a year of global daily precipitation data and uniform quality data sets extending up to (near) planetary scales are available hourly from geostationary satellites. Clouds and rain are strongly nonlinearly coupled, so that if the scale invariant symmetry is broken in the cloud field, it will almost certainly be broken in rain too (and presumably visa versa). Note that this argument does not imply the existence of one-to-one relations between the various fields, nor—since their types of scalings are expected to be different—does it even imply that the statistics are the same. Cloud radiances have the advantage that unlike in situ gauge data, they are largely unbiased by network homogeneity or problems of rainrate dependent rain gauge resolution (especially for low rain rates; see (De Lima, 1998)). In addition, radar can (and should) be used for studying scaling although it measures microwave backscatter not rain rate and the disadvantage that for scales larger than that of a single radar ($\approx$200 km) that radar networks are required. However, the correct handling of overlapping radar images is itself non-trivial (due to the range and resolution dependence of the statistical properties). Although satellite radar (TRMM) does overcome the network problem, it measured microwave backscatter only over a very narrow swath ($\approx$10 km) and relied on visible, infra red and passive microwave radiances to infer areal rainfall.

2.2. The data

In terms of the information content, the largest existing scaling cloud study (Lovejoy et al., 1993) analyzed only 15 cloud scenes (five wavelengths each) over a period of less than a month—not long enough to sample the full large scale variability. In order to extend this study, we obtained data from the archives of the Atmospheric Radiation Measurement (ARM) programme from of three satellites each with infra red and visible channels. These images are physically quite different since the visible is essentially multiple scattered cloud and surface solar radiation whereas the infra red data are essentially unscattered thermal blackbody radiation (for the channels discussed here, we may neglect direct solar contributions). The primary data set consisted of scenes over the ARM Oklahoma test site from the sun-synchronous NOAA-12 and NOAA-14 satellites' Advanced Very High Resolution Radiometer (AVHRR) sensor subscenes centered over Wichita Kansas (see Table 1). In addition, a smaller set of geostationary GMS-5 images over the central Pacific were also used. The GMS data were taken within a month of each other and so were less representative of the meteorological variability, but had the advantage of extending the range of scales to over 5000 km (only the central 1024×1024 pixel square was used in order to minimize cartographic distortion).

Since, it is important that the sample of images be as unbiased as possible, some comments are in order. To begin with, images were not received every day. In addition, some scenes were not used because of artifacts (such as missing lines) or because the sun had not risen (visible data only; this accounts for most of the rejections for the winter NOAA 12 data; see Table 1). Many pictures had isolated pixels with clearly spurious values; these, however, were generally corrected by replacing them with the average of their neighbors. Also, for the visible data, a sun and satellite angle correction was used. This consisted of normalizing the raw radiances by the cosines of the zenith angles of each (this correction would be exact for a Lambertian reflector). Since, for any individual image, this correction was taken as a constant, it does not affect the scaling. However, for the ensemble spectrum, it gives a more equal weight to each picture in the ensemble.

2.3. The isotropic scaling

Spectral analysis is a sensitive way of performing scale by scale analysis and it has the additional advantage that it is relatively familiar to geophysicists. The isotropic energy spectrum $E(k)$ (k is the modulus of a wavevector) is defined as the angle integrated ensemble average of the square fourier modulus of the data. Isotropic scaling implies: $E(k)=k^{-\beta}$, where β is the 'spectral exponent'. Angle integration is preferred to angle averaging since in an isotropic system the resulting exponent β will be the same on subspaces (e.g. on linear sections of the images; the difference between integration with respect to averaging is $2\pi k$, $4\pi k^2$ in 2D and 3D, respectively). In addition to the minimal pre-processing indicated in Section 2.2, we applied standard Hanning filters. Clearly this standard use of isotropic

Table 1
The characteristics of the data used in this study

Satellite, channel	Wavelength (μm)	Resolution, scene size (km)	Period covered	Local time ±30′	Images used/total
NOAA 12, channel 1	0.58–0.68	1.1, 280	30/1/96–20/1/97	19:30, 8:00	134/156
NOAA 12, channel 5	11.5–12.5	1.1, 280	30/1/96–11/2/97	19:30, 8:00	353/354
NOAA 14, channel 1	0.58–0.68	1.1, 280	30/1/96– 4/2/97	14:30, 3:00	150/162
NOAA 14, channel 5	11.5–12.5	1.1, 280	30/1/96–7/10/96	14:30. 3:00	211/214
GMS-5 visible	0.5–0.75	5, 5120	13/3/96–15/4/96	Noon, sub satellite	29/29
GMS-5 IR	10.2–12.5	5, 5120	13/3/96–15/4/96	Noon, sub satellite	29/29

The NOAA images were remapped onto a Mercator projection.

spectra ‘washes out’ much of the anisotropy; below we argue that it is precisely this (presumably scaling) anisotropy which largely accounts for the differences between different images, different cloud morphologies, different cloud types.

Typical individual spectra are shown in Fig. 1a; the variation about the log–log linear (power law) behaviour is small and—as shown by numerical multifractal simulations (Section 3), is of the order expected by purely random causes. This is plausible if we recall that a straight line is only expected on an ensemble average; on the contrary on any single realization of a scaling process, the scaling will almost surely be broken, it can only be approximately linear. The other sensors, other wavelengths gave comparable results. To check for any possible seasonal variation, we display Fig. 1b which shows that the scaling is well respected on a monthly basis with little noticeable systematic change from month to month. Note that here and in the following, no attempt was made at an absolute calibration.

Due to the good isotropic scaling, we proceeded to estimate the ensemble (isotropic) statistics see Fig. 2a and b for NOAA 14 satellite and Fig. 2c for an intercomparison of the NOAA 12 with GMS. The only strong break visible is at the small scale end of the GMS 12 IR data. Since, none of the other channels (including the NOAA 12 and 14 at the same scales) showed this feature, we concluded that this was an artifact of a slight oversampling on the GMS IR sensor. For the subsequent analyses we averaged and resampled this channel by a factor of 2 in order to minimize this effect. Finally, in Fig. 3 we compare visible spectra for GMS, NOAA-12, a single SPOT image (over France) and the average of 38 ground based photographs discussed in Sachs et al. (2002). Although the exact slopes differ—we argue below because of the differing surfaces/backgrounds which affect radiances—the basic isotropic scaling is excellent over the entire range of 5000 km down to 1 m. We quantify this statement in Section 4. Note that over the land, the bidirectional reflection coefficient and infra emission is also apparently scaling (e.g. Gaonac’h et al., 1999; Laferrière and Gaonac’h, 1999) as is the topography (e.g. Gagnon et al., 2003) so that a priori, the surface features do not break the scaling.

3. Multifractal models of rain and clouds

3.1. Cascade properties

Non-linear scale invariant processes have dynamical mechanisms that repeat scale after scale from large to small; they are cascade-like. In the last 20 years, it has become clear that cascades are the generic scale invariant multifractal process and can thus generally serve as multifractal models—at least of conservative scaling processes (see below). We will illustrate them using the example of the turbulent energy flux ε. Since, the 1980s, cascades have been used for rainfall modeling by many authors including (Veneziano et al., 1996; Over and Gupta, 1996a; Mazzarella, 1999; Deidda, 2000). Consider a discrete in scale cascade such as that shown in Fig. 4 developed over total scale ratio $\lambda = L/L_d$, L being a large external scale, L_d the small dissipation scale. The kinetic energy flux of ‘daughter eddies’ is multiplicatively modulated by ‘parent’ eddies at each (factor 2) cascade step, giving rise to potentially huge fluctuations. If each cascade step is over scale ratio λ_0, after

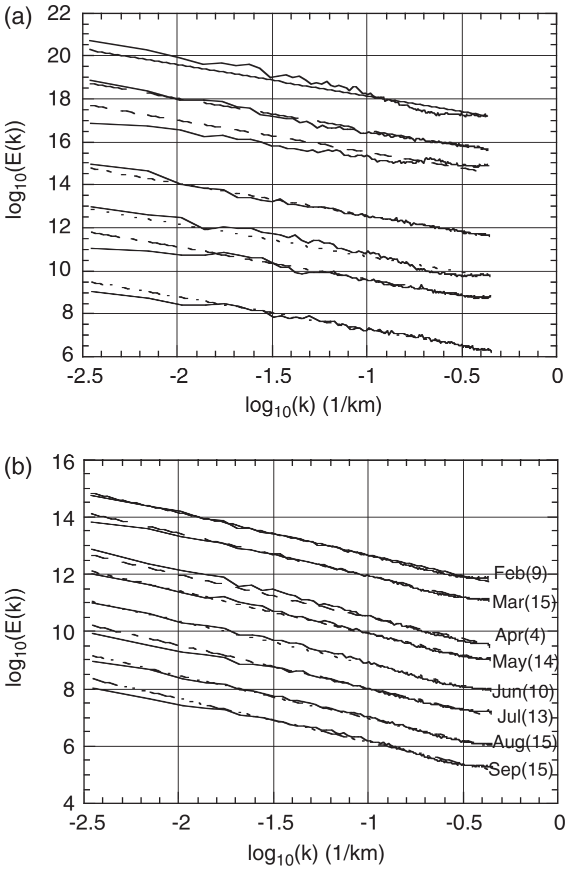

Fig. 1. (a) The isotropic spectra of every second NOAA-12 (AVHRR) visible images obtained in May, 1996 are shown here displaced from each other. The straight reference lines all have a slope equal to the average spectrum for all 134 images ($=-1.57$). Recall that the isotropic energy spectrum gives the contribution to the overall variance (integrated over all directions) due to structures with wavenumbers between k and $k+\mathrm{d}k$. From top to bottom the dates of the images are 1, 3, 8, 11, 15, 21, and 30 May. The fact that the isotropic spectra are very similar does not imply that the scenes are necessarily similar since the scale by scale anisotropies are generally quite different corresponding to different cloud types. The slopes $\beta=1-K(2)+2H$. Since $K(2)$ is small and varies little (see the small C_1, α and small variations in Fig. 6), most of the variations in slope are due to variations in H. (b) The average spectrum for eight months' NOAA-12 (AVHRR) visible data is shown here (1996). The spectra are all displaced from each other and each month is indicated, along with the number of images' spectra used in the average (indicated in the parentheses), next to the relevant plotted data. Each spectrum is shown for comparison next to a line of slope -1.57 (=the average slope over all 134 images used).

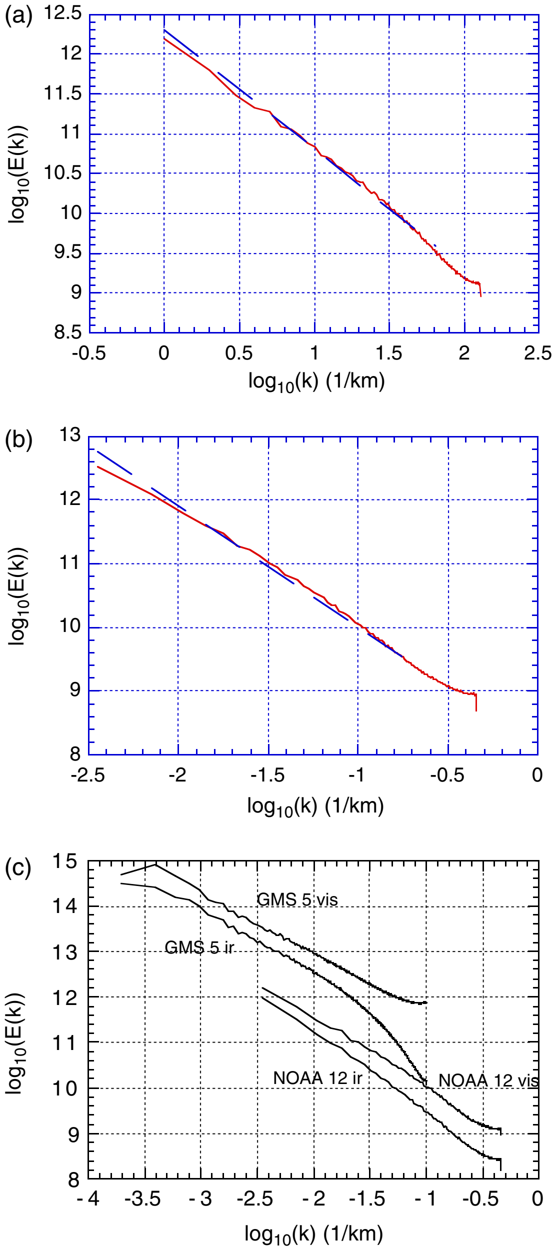

Fig. 2. (a) This is the average (isotropic) energy spectrum of 158 NOAA-14 (AVHRR) images, channel 1 (0.58–0.68 μm), taken from January to September, 1996. As for NOAA-12, the resolution is 1.1 km and the images are 256×256 pixels. The regression slope is -1.50. All images are taken between 1930 and 2030, GMT, over the ARM SGP site. (b) This is the average energy spectrum of 209 NOAA-14 infrared images, channel 5, taken from January 1996 to October 1997. The images were all taken at approximately 2030 or 0900 GMT, over the ARM SGP site. The images were taken using

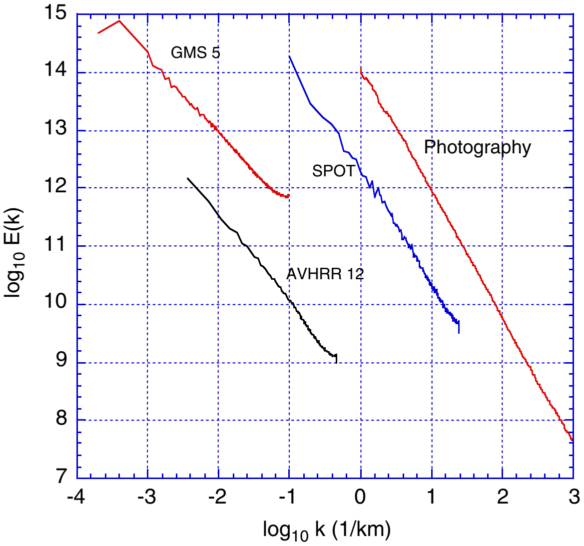

Fig. 3. The average spectra obtained for the GMS, NOAA 12, data discussed in Section 2, as well as a SPOT (20 m resolution) image over France, are shown here together for comparison (displaced in the vertical for clarity). The GMS spectrum shows a range of scales of 5120–10 km, the NOAA 12 spectrum shows a range from 256 to 2 km and the SPOT spectrum shows a range from 10 km to 40 m. At the far right we also show the average of 38 ground based pictures (some with resolutions of 50 cm, this is the average of the data discussed in Sachs et al. (2002)). As indicated in Table 3b, the main differences are in H, i.e. in the 'roughness'. This is strongly influenced by the background; it is not surprising that the largest *H* and steepest spectra (smoothest images) are from the ground looking up with smooth sky background.

n steps we have the following energy flux density ε_n:

$$\varepsilon_n = \prod_{j=1}^{n} \mu\varepsilon_j \tag{1}$$

where $\mu\varepsilon_j$ is the 'multiplicative increment' due to the jth step (the initial energy injected ε_0 is assumed unity for simplicity). After n steps, with $\lambda = \lambda_0^n$ (the total scale ratio (large/small) over which the cascade has been developed), the statistical moments follow:

$$\langle \varepsilon_\lambda^q \rangle = \lambda^{K(q)} \tag{2a}$$

where $K(q)$ is the moment scaling function. The corresponding probabilities follow:

$$\Pr(\varepsilon_{\lambda>} > \lambda^\gamma) \approx \lambda^{-c(\gamma)} \tag{2b}$$

(Schertzer and Lovejoy, 1987b), where $c(\gamma)$ is the statistical codimension of the singularity $\gamma = \log \varepsilon_\lambda / \log \lambda$ and the '≈'means equality to within log corrections (see Section 4 for more discussion of these). $\langle \varepsilon_\lambda^q \rangle$ and $\Pr(\varepsilon_{\lambda>} > \lambda^\gamma)$ are related by a Mellin transform (Schertzer and Lovejoy, 1992), the exponents $K(q)$, $c(\gamma)$ via a Legendre transformation, (Parisi and Frisch, 1985):

$$\begin{aligned} K(q) &= \min_\gamma(q\gamma - c(\gamma)); \\ c(\gamma) &= \min_q(q\gamma - K(q)) \end{aligned} \tag{3}$$

hence there is a one to one relation between singularities and statistical moments: $\gamma = K'(q)$, $q = c'(\gamma)$ so that for large λ, a single γ gives the dominant contribution to each moment order q.

The small scale limit ($\lambda \to \infty$) of such a cascade is highly singular. In particular, we note the logarithmic divergence of the log moments with scale: $\log\langle \varepsilon_\lambda^q \rangle \approx K(q) \log \lambda$. It is this systematic resolution dependence which makes the behaviour of mulifractals very different from that of classical geophysical fields: the latter are predicated on various assumptions about the mathematical regularity of the fields which at first sight appear plausible, but which in fact turn out to be highly restrictive. In particular, multifractal measures are singular with respect to the standard Lebesgue measures. This implies for example that rain and cloud areas do no converge as they are measured at finer and finer resolution. In order for any mathematical convergence properties to exist, constraints must be imposed on the cascade. The two basic alternatives for the energy conservation are that it does so locally in space—yielding a microcanonical cascades or conservation only over ensemble averages, yielding canonical cascades. In microcanonical cascades, $\gamma < \gamma_{\max}$, where $\gamma_{\max}$ is an upper bound introduced by the microcanonical constraint; if the latter is imposed on a space of dimension D, then $\gamma_{\max} < D$ (Schertzer and Lovejoy,

◀

the infrared channel 5 (11.5–12.5 μm) with a resolution of 1.1 km. All images are 256×256 pixels. The regression slope is −1.88. (c). Comparison of the average infrared and visible spectra for GMS-5 and NOAA-12. Here, the visible and infrared GMS-5 spectra both make use of 29 images. The visible NOAA-12 data makes use of 134 images, the infrared of 353 images. The extreme high frequency ends suffer from noise (flattening) except the GMS IR which dips down due to oversampling.

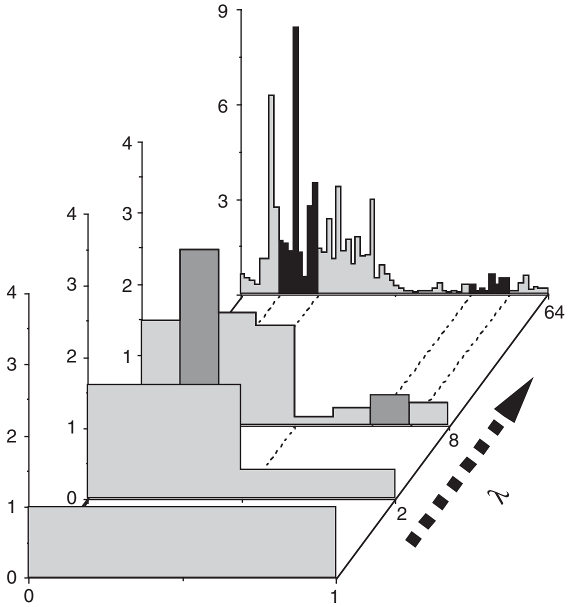

Fig. 4. A schematic showing one dimensional multifractal ‘α model’ cascade at various stages in its construction, obtained by allowing for boosts and decreases in energy flux density (vertical) axis (the integral of which is conserved on average during the cascade). At each step the horizontal scale is divided by two, and independent random factors are chosen either greater or less than one normalized so that the average is one, *l* is the ratio of the outer scale (L = unity here) to the small scale of the resolution ($\eta = 1/\lambda$).

1992). Using $\gamma < \gamma_{\max}$ in the Legendre transformation (Eq. (3)) we find the following discontinuity in the slope of $K(q)$ (‘multifractal phase transition’):

$$K(q) = q\gamma_{\max} - c(\gamma_{\max}); \qquad q \ge c'(\gamma_{\max}) \tag{4}$$

Cast in a slightly different setting (and with the micro-canonical assumption only implicit), (Novikov, 1970) obtained the corresponding inequalities on the statistical moments $\langle \mu\varepsilon_\lambda^q \rangle$; these ‘Novikov’ inequalities therefore do not apply to canonical cascades. Note that since any finite sample has a largest singularity (even if the process itself will eventually generate singularities of all orders), this leads to a linear asymptote on $K(q)$ called a ‘multifractal phase transition’ (Schertzer and Lovejoy, 1992).

In comparison, the less restrictive canonical cascades only impose conservation on ensemble averages, (i.e. $\langle \mu\varepsilon \rangle = 1$) and they generally have no upper bound on the singularities. While the canonical cascades are more general and (apparently) more physically appropriate (see below), the small scale limit is non-trivial. It turns out that there is indeed no small-scale limit ($\lambda \to \infty$) in the sense of functions (i.e. at mathematical points), but only in the weak sense of measures (i.e. in the neighborhood of points); only integrals over finite sets of dimension D have any convergent statistics. In general as first pointed out by (Mandelbrot, 1974) there will be a critical order of divergence q_D such that:

$$\Pr(\varepsilon_{\lambda>} > s) \approx s^{-q_D}; \qquad \langle \varepsilon_\lambda^q \rangle \to \infty; \quad q \ge q_D \tag{5}$$

See Tables 2a and b for an intercomparison of various cascade types.

In rain values q_D near three have been found (see the review (Lovejoy and Schertzer, 1995b), also (Tessier et al., 1996; Bendjoudi et al., 1997; De Lima et al., 2001, 2004); in rivers, there is more variation in q_D so that it is not clear that a unique value can be used (see Turcotte and Greene, 1993; Tessier et al., 1996; Pandey et al., 1998; Hubert et al., 2001). In addition, the value $q_D = 3$ is predicted theoretically on the basis of a compound multifractal Poisson process (Lovejoy and Schertzer in preparation). Because this extreme algebraic behaviour is excluded from microcanonical (and also bounded) cascades, this growing empirical evidence for algebraic tails of the probabilities is primae facae evidence for canonical cascades. Note that additive processes with algebraic probability tails (involving Levy distributions) cannot account for values of $q_D \ge 2$ and are thus also excluded. Tables 2a and b compares and contrasts various multifractal models.

3.2. Universality and continuous in scale cascades

3.2.1. Universality

In general, canonical cascades lead to statistics characterized by a convex $K(q)$; this is equivalent to knowledge of an infinite number of theoretical or empirical parameters. Hence, without further assumptions, modeling and analysis would be impossible. This is the problem of ‘universality’ familiar to physicists. In the case of multifractals, due to the technical difficulties surrounding the non-trivial singular small scale limit, the debate about universality was complicated. It is now clear that in principle (i.e. mathematically) universal multifractals do exist, see the debate (Schertzer and Lovejoy, 1997). The key

Table 2a
This table compares and contrasts statistical exponents displayed by various discrete in scale cascade processes, i.e. those that are based on integer scale ratios

	$c(\gamma)$	$K(q)$	$\xi(q)$
Micro-canonical[a]	$\gamma \le \gamma_{\max}$; $\gamma_{\max} \le D$	$K(q) = q\gamma_{\max} - c(\gamma_{\max})$; $q \ge c'(\gamma_{\max})$	$\zeta(q) = qH - K(q)$ any H
Canonical[b]	$c > 0$, c is convex	K is convex; $K(q) \to \infty$; $q > q_D$	$\zeta(q) = qH - K(q)$ any H
Bounded cascade and additive truncated cascade[c]	$c_b(\gamma) = \frac{\gamma}{H}$; $\gamma < H$ $c_b(\gamma) = \infty$; $\gamma \ge H$ $H > 0$	$K_b(q) = 0$; $q < 1/H$ $K_b(q) = qH - 1$; $q > 1/H$	$\xi(q) = qH$; $q < 1/H$ $\xi(q) = 1$ $q \ge 1/H$
Iterated function systems[d]	$c(\gamma) = 1 + x\log_2 x + (1-x)\log_2(1-x)$; $x = \left(\frac{\gamma - \gamma^+}{\gamma^+ - \gamma^-}\right)$ $-1 < \gamma^- < \gamma^+ < 1$	$K(q) = q\frac{(\gamma^+ + \gamma^-)}{2} + \log_2 \cosh\left(q\frac{(\gamma^+ - \gamma^-)}{2}\log 2\right)$	$\zeta(q) = qH - K(q)$; $H = -\log_2 \lvert d\rvert - \frac{(\gamma^+ - \gamma^-)}{2} - \log_2 \cosh\left(\frac{(\gamma^+ - \gamma^-)}{2}\log 2\right)$ $\lvert d\rvert < 1$

Presumably realistic cascades require this ratio to tend to unity, they are continuous in scale (see Table 2b).

[a] The structure function exponent is given for the Fractionally Integrated Flux model; i.e. after the cascade is fractionally integrated by an order H.

[b] In general, $c(\gamma)$ becomes linear due to the divergence of moments (Eq. (6)) so that $K(q)$ diverges for $q > q$D.

[c] The basic result for the structure function is given in Cahalan (1994); the results from $c(\gamma)$, $K(q)$ follow from it. The truncated additive cascade is obtained by adding rather than multiplying; when it is truncated so as have only $c < 1$ (implicit in the discrete bounded multiplicative cascade), it has the same exponents.

[d] The basic result for the structure function is given in Levy-Véhel et al. (1995), here we give the $c(\gamma)$, $K(q)$ which follow from it. Note the restrictions on the parameter ranges.

Table 2b
To our knowledge, these are the only continuous in scale cascades models which have been proposed in the literature

	$c(\gamma)$	$K(q)$	$\xi(q)$
Universal (log-Levy), fractionally integrated flux[a]	$c(\gamma) = C_1\left(\frac{\gamma}{\alpha' C_1} + \frac{1}{\alpha}\right)^{1/\alpha'}$; $\gamma < \gamma_D$; $c(\gamma) = q_D(\gamma - \gamma_D) + c(\gamma_D)$; $\gamma > \gamma_D$ $\frac{1}{\alpha} + \frac{1}{\alpha'} = 1$ $0 \le \alpha \le 2$	$K(q) = \frac{C_1}{\alpha - 1}(q^\alpha - q)$; $q < q_D$ $K(q) = \infty$; $q > q_D$	$\zeta(q) = qH - K(q)$ any H
Poisson[b]	$c(\gamma) = \left(1 - \frac{\gamma^+ - \gamma}{c\gamma^-}\left(1 - \log\frac{\gamma^+ - \gamma}{c\gamma^-}\right)\right)c$; $\gamma \le \gamma^+$; $c(\gamma) = \infty$; $\gamma > \gamma^+$; $\gamma^- = \log\left(1 - \frac{\gamma^+}{c}\right)$; $c = c(\gamma^+)$	$K(q) = q\gamma^+ - c + \left(1 - \frac{\gamma^+}{c}\right)^q c$	$\zeta(q) = qH - K(q)$
Attenuated cascade (nonscaling)[c]		$K(q) \approx \frac{C_1}{\alpha - 1}(q^\alpha - q)\left(\frac{1 - e^{-\kappa w}}{\kappa w}\right)$ $\kappa = \frac{\log \lambda}{\log \Lambda} \le 1$	

Note that only the Universal FIF model has unbounded singularities as required in systems displaying power law tails of probability distributions.

[a] We give the $c(\gamma)$ corresponding to the divergence of moments (Eq. (5)); $\gamma_D = K'(q_D)$. For $K(q)$ we give the result for an infinite ensemble; for finite ensembles, there will be a discontinuity in the slope of $K(q)$ at q_D, after which $K(q)$ is linear with slope dependent on the sample size.

[b] This was first proposed in She and Levesque (1994) and applied to rain by Deidda (2000). The maximum singularity γ^+ and corresponding codimension $c = c(\gamma^+)$ can be chosen fairly arbitrarily, see the discussion in Schertzer et al. (1995).

[c] This model is not scaling due to the λ dependence in the κ parameter; w characterizes the attenuation of the cascade over the range Λ ($> \lambda$) over which the continuous attenuated cascade is defined.

outstanding issue is the relevance of the proposed routes to universality in rain. However, one of the proposed routes is the 'densification' of the cascade spectrum by making the cascade continuous in scale, i.e. by taking the limit of the step ratio $\lambda_0 \to 1$ (Schertzer and Lovejoy, 1987a). This is presumably physically realistic—certainly there is no physical basis for cascades with discrete integer step scale ratios λ_0. Mathematically, continuous in scale multifractals have 'infinitely divisible' generators.

Universal multifractals are the multiplicative analogues of the (additive) central limit theorem, they lead to mulitfractals with Levy generators and the exponents:

$$K(q) = \frac{C_1}{\alpha - 1}(q^\alpha - q) \tag{6a}$$

$$c(\gamma) = C_1\left(\frac{\gamma}{\alpha' C_1} + \frac{1}{\alpha}\right)^{1/\alpha'}; \qquad \frac{1}{\alpha} + \frac{1}{\alpha'} = 1 \tag{6b}$$

where C_1 is the codimension of the mean and $0 \le \alpha \le 2$ is the Levy index of the generator. $\alpha = 0$ corresponds to the monofractal 'beta model', $\alpha = 2$ to the 'log-normal' multifractal. Note that due to the singular small scale limit, the above will generally only hold up the a critical upper limit q_D discussed above.

A useful property of universal multifractals which we will exploit below is the scaling of the normalized η power:

$$\langle (\varepsilon_\Lambda^\eta)_\lambda^q \rangle = \lambda^{K(q,\eta)} \tag{7}$$

where the notation indicates that the field ε is taken at its finest resolution and raised to the η power; the result is degraded to resolution λ and the mean q power is taken. The exponent $K(q,\eta)$ depends on both η and q, it is related to the usual $K(q) = K(q,1)$ as follows:

$$K(q,\eta) = K(q\eta) - qK(\eta) \tag{8}$$

This result is quite general, however, in the special case of universal multifractals (Eq. (6a)), the above simplifies and we obtain:

$$K(q,\eta) = \eta^\alpha K(q,1) \tag{9}$$

This means that by comparing the scaling for various η values with exponent q fixed, we can directly estimate α (and hence C_1) by linear regression of log $K(q,\eta)$ vs. log $K(q,1)$. This is the 'Double Trace Moment' (DTM) technique (Lavallée et al., 1993) which is simpler and more robust than directly estimating the parameters from $K(q)$ (Eq. (6); especially since this universal form is only valid for q below a critical value q_D determined by the multifractal phase transitions mentioned above).

3.2.2. Continuous in scale multifractals

The original approach for making continuous in scale multifractal models with statistics governed by Eq. (6)—the Fractionally Integrated Flux (FIF) model—were first described in (Schertzer and Lovejoy, 1987a). They were later extended to down-scaling in (Wilson, 1991), to linear generalized scale invariance in (Wilson, 1991), (Pecknold et al., 1993) to causal space–time modeling in (Marsan et al., 1996; Schertzer and Lovejoy, 1997). The first step in making an isotropic FIF model in D dimensional space is to make the continuous in scale, conservative multifractal process. We start with an (appropriately normalized) noise subgenerator $\gamma(\underline{X})$ made by distributing i.i.d extremal Levy random variables on the simulation grid; $\underline{X} = (x, y, z)$ for a spatial model $L, \underline{X} = (\underline{x}, t)$ for a space–time model. This is then fractionally integrated to yield the generator $\Gamma(\underline{X})$, exponentiated to yield the conservative cascaded flux $\varepsilon(\underline{X})$ and again fractionally integrated again to yield the rain rate R:

$$\Gamma(\underline{X}) \propto C_1^{1/\alpha}\gamma(\underline{X}) * |\underline{X}|^{-(D-1/\alpha)}; \qquad \varepsilon(\underline{X}) = \mathrm{e}^{\Gamma(\underline{X})} \tag{10}$$

where '*' indicates 'convolution'.

'Weakly universal' multifractals have been proposed based on Log-Poisson generators (She and Levesque, 1994). They have been recently been applied to rain (Deidda, 2000); see Table 2 for the statistics). However, while log Poisson processes are continuous in scale, they are neither stable nor attractive, hence they are at best 'weakly universal'. In addition, they have an intrinsic upper bound on the singularities they can generate so that q_D is generally infinite, a restriction that seems incompatible with the finite q_D observed in rain rate distributions; see also (Schertzer et al., 1995) for an empirical assessment of Log-Levy vs. Log-Poisson distributions in turbulence.

3.3. Nonconservative multifractals

So far the multifractals we have described are the direct outcome of multiplicative cascades; they have non-linear scaling exponents with $K(1)=0$ due to the conservation constraint. In general, the observable fields have additional (linear) scalings, the prototypical example being the turbulent velocity field v:

$$\Delta v(\Delta x) = \varepsilon^a \Delta x^H \tag{11}$$

In turbulence, the Kolmogorov values are $a=H=1/3$, and taking absolute values and averaging, we obtain the 'qth order structure function':

$$\langle|\Delta v(\Delta x)|^q\rangle = \Delta x^{\zeta(q)}; \qquad \Delta v(\Delta x) = v(x+\Delta x) - v(x) \tag{12}$$

where $\zeta(q)$ is the structure function exponent (the statistics are assumed to be translationally invariant i.e. independent of x). Taking for simplicity $a=1$, and using $\Delta x \propto \lambda^{-1}$ we obtain:

$$\zeta(q) = qH - K(q) \tag{13}$$

when $\zeta(q)$ is linear, $K(q)$ is either zero or is itself linear; in either case, the system is 'monofractal' otherwise it is concave, and the system is multifractal.

A final result useful below for estimating H, is the relation with the spectrum; using the Wiener–Khintchin theorem (which relates the autocorrelation to the spectrum via a fourier transform), we find:

$$\beta = 1 + \zeta(2) = 1 + 2H - K(2) \tag{14}$$

Since, $K(2) \geq 0$, this shows that for conservative cascades ($H=0$), $\beta \leq 1$.

3.4. Models of nonconservative multifractals

3.4.1. Fractionally integrated flux model (FIF)

There are several ways of modeling a nonconservative multifractal field (sometimes called 'synthetic turbulence'; see Table 2). The first and still most general is the FIF model which simply uses fractional integration of order H of a conservative flux ε, we have (see e.g. Schertzer and Lovejoy, 1987a, 1997):

$$v(\underline{X}) = \varepsilon(\underline{X}) \times |\underline{x}|^{H-\mathrm{D}} \tag{15}$$

where D is the dimension of space. The resulting field v satisfies Eqs. (11) and (12). In the above, the space–time vector norm $|\underline{X}|$ is isotropic; the result is a self-similar multifractal.

3.4.2. Additive cascade

A number of proposals have been made in order to directly model a nonconservative field without first modeling a conservative multifractal. Although—unlike the cascade models and FIF—no serious attempt has been made to give them a physical basis, they have been applied to rain and turbulence modeling. In order to understand some of these, we first discuss the simple additive cascade which—when truncated—turns out to be essentially identical to the multiplicative bounded cascade (Section 3.4.3) only it is much simpler to analyze.

In analogy to Eq. (1), consider the following additive cascade over a hierarchical 1D grid with cascade step $\lambda_0=2$:

$$\varepsilon_n = \sum_{j=1}^{n} \delta\varepsilon_j \tag{16}$$

where the additive increments are:

$$\delta\varepsilon_j = \pm f c^j \tag{17}$$

and $0<c\leq 1$, $0<f\leq 1$ are model constants and the ± signs are taken randomly with equal probability so that $<\delta\varepsilon_j>=0$. This is very similar to the midpoint displacement algorithm (Fournier et al., 1982), close to a fractional Brownian motion with parameter $H=-(\log c/\log 2)$, It results in a linear structure function exponent. When the process is truncated so that $c(\gamma)<1$, it yields piecewise linear exponents (Table 2a) identical to the bounded cascade discussed below.

3.4.3. Bounded cascade

We start with a two-state, one-dimensional model, with elementary cascade steps of ratio $\lambda_0=2$. In the model there are only two possible states per cascade step and the energy flux is exactly conserved at each step (it is microcanonical) with multiplicative increment:

$$\mu\varepsilon_j = 1 \pm f c^j \tag{18}$$

with again $0\leq f\leq 1$, $0\leq c\leq 1$. The energy flux is multiplicative following Eq. (1).

This 'bounded cascade' was inspired by (Bell, 1987) who weakened the cascade at small scales (but in a somewhat different way) in order to avoid the singular small scale limit. Although (Schertzer and Lovejoy, 1987a) showed how this limit could be tamed without any kind of bounding, (Cahalan, 1994) nevertheless proposed the above bounded cascade (it was applied to rainfall by (Menabde et al., 1997)). Note that if $c=1$ we retrieve the microcanonical 'p model' (Meneveau and Sreenivasan, 1987b), itself a microcanonical restriction of the canonical two-state 'α model' (Schertzer and Lovejoy, 1985a). The statistics are shown in Table 2a; in the small scale limit they are identical to the truncated additive cascade so that its multiplicative construction is somewhat misleading (they are a bit different at the largest scales). For comparison with a continuous cascade, in Table 2b we give the exponents for a continuous in scale 'attenuated' cascade whose singularities are algebraically reduced per cascade step.

3.4.4. Iterated function systems (IFS) multifractals

An approach originally developed for modeling geometrical fractal sets is the Iterated Function System (IFS) approach proposed by (Barnsley, 1993), developed by (Levy-Véhel et al., 1995) and applied to turbulent systems by (Basu et al., 2004). To produce an IFS system one starts with one or more initiators and (self affine) linear transformations. By iteratively transforming and taking unions of the resulting sets one can produce a huge range of geometric fractal sets. In order to use the method to produce 1D fractal functions (e.g. $R(t)$), one produces a set and interprets the result as the graph of a function. For this to provide a useful model, special parameter values must be used so that the result is single valued. (Levy-Véhel et al., 1995) and (Basu et al., 2004) propose a specialization of the IFS process based on factor of λ_0 discrete scale ratios that results in the statistical exponents shown in Table 2. The IFS and bounded cascades only give very special types of $c(\gamma)$, $K(q)$, $\xi(q)$'s and their discrete in scale construction implies the unrealistic feature of being only exactly scaling for integer powers of λ_0.

3.5. Numerical simulations of FIF

3.5.1. The parameters for rain and clouds

There have been a number of empirical estimates of the parameters C_1, H, α for rain (Lovejoy and Schertzer, 1990; Tessier et al., 1993, 1996; De Lima, 1998; see the review Lovejoy and Schertzer, 1995b). The primary difficulty is undoubtedly the extreme, nonclassical variability discussed in Section 3.5.2; however, there is an additional problem which is important in modeling and analysis; the problem of the zeroes. Empirically, the zeroes greatly affect the low rain rate statistics, hence methods for estimating the multifractal index α which typically exploit the nonanalyticity of $K(q)$ near $q=0$) will be sensitive to the way the measuring instrument handles the problem. This may explain the various published estimates with α in the range from 0.5 to 0.8 (time, Ladoy et al., 1993; De Lima, 1998; Labat et al., 2002) and 1.35–2 for the horizontal direction in space (Tessier et al., 1993; Chigirinskaya et al., 2002; Biao, 2003; Duncan, 1993). Theoretically, there are basically two ways to handle the zeroes: (a) by using two processes; the first to determine the support (i.e. the nonzero regions), the second, the rainrate on the support, (b) by using a single process to determine rain rates everywhere, but to introduce a threshold below which the rain rate is set to zero. Although the difference between the approaches may seem to be somewhat academic, it is not: in general, method (b) introduces a characteristic length/time in rain. In the compound multifractal Poisson rain model the issue is taken care of in a more physical way via the drop number density field (Lovejoy and Schertzer in preparation). In what follows, for simplicity—and because the basic issue is unresolved—we use the threshold method which can be derived as an approximation to the multifractal compound Poisson model. Note that since most measuring devices have minimum detectable signals, they can introduce spurious length scales and may account for a number of otherwise contradictory observations.

Fig. 5a and b shows an example of FIF cloud and rain simulations the result using parameters estimated for rain (5a), clouds (5b). Fig. 5c shows how three dimensional simulations of liquid water density with realistic differential stratification in the vertical can be used to simulate radiation fields in the visible, infra red. In this way they can simulate satellite rain algorithms (e.g. RAINSAT, Lovejoy and Austin, 1979; Bellon et al., 1980) which use infra red radiances to distinguish high (cold) and low (warm) cloud tops, and visible radiances to distinguish thin and thick clouds; the two are used to estimate the probability of rain (as determined by radar). For more examples of multifractal simulations, see http://www.physics.mcgill.ca/~gang/multifrac/index.htm.

3.5.2. *Extensions to anisotropy, causality*

Since, scaling in real systems is never exactly isotropic (self-similar), for applications we must extend the FIF to anistropic scaling. In the above, $\underline{X}=(x, y, z, t)$, i.e. we consider at the outset the

(a)

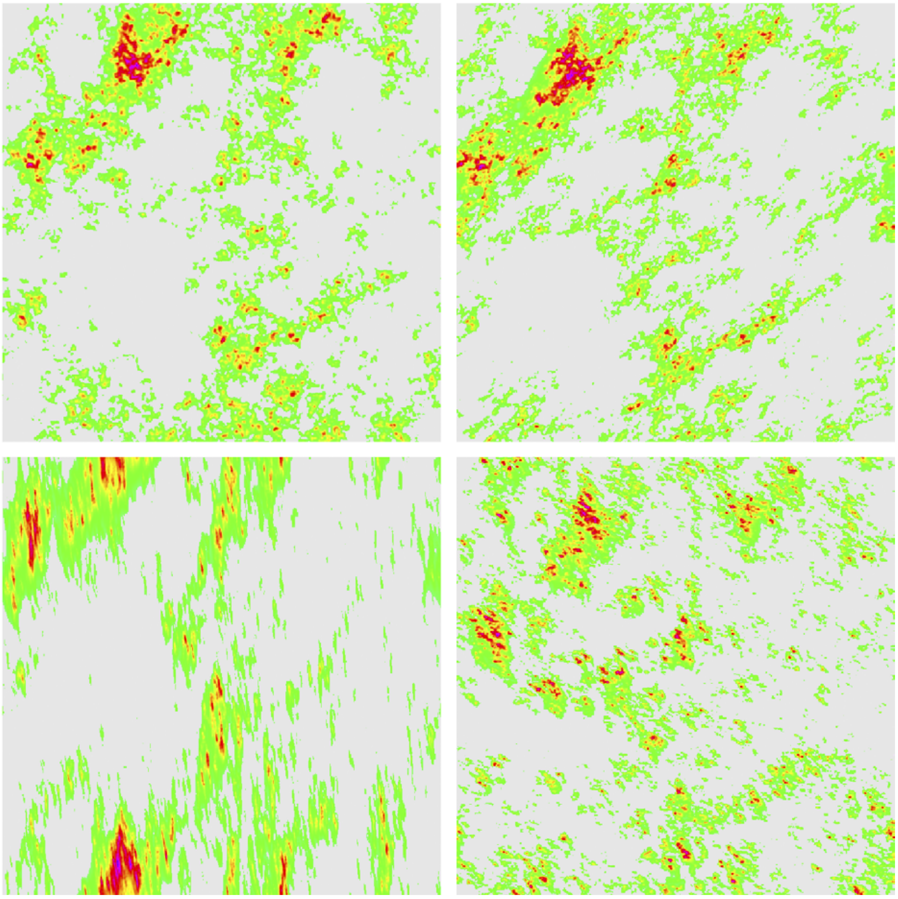

Fig. 5. (a) This figure shows the effect of varying the anisotropy on 512×512 pixel rain simulations ($\alpha=1.5$, $C_1=0.2$, $H=0.1$; note this is a log scale so as to mimick a radar representation the parameters are close to those estimated in (Tessier et al., 1996)). At the top left we have both an isotropic generators ($G=$identity) and all scales are isotropic. At the top right (with same random seed so that the structures can be compared), we retain the isotropic generator, but allow the unit scale to be deformed; however, the deformation (anisotropy) is the same at all scales these two cases are thus ‘self-similar’ multifractals, the anisotropy is ‘trivial’, i.e. the same at all scales, on the lower left we have a stratification dominant case (i.e. G has real eigenvalues) with $\mathrm{G} \; = \; = \begin{pmatrix} 0.7-0.1 \\ 0.1 \quad 1.3 \end{pmatrix}$. The sphero-scale (i.e. the scale at which structures are roughly isotropic) is $l_s=256$ pixels. On the right is a rotation dominant case (i.e. G has complex eigenvalues) with $\mathrm{G}=\begin{pmatrix} 0.7-1 \\ 1 \quad 1.3 \end{pmatrix}$. Note that the differences in the simulations are at all scales, they are due to a difference in the notion of scale itself. Our hypothesis is that effects of convection and other meteorological processes would modify the scale function while retaining the basic statistical multifractal exponents (α, C_1, H). (b). This is identical to (a) (including random seed) except that is cloud parameters $\alpha=1.9$, $C_1=0.075$, $H=0.36$, have been used and the colouring scale is linear (from blue to bright white). (c). Three dimensional cloud simulations (on 256×256×128 point grids) with liquid water density (LWC) close to those observed in aircraft ($\alpha=1.8$, $C_1=0.1$, $H=0.33$). Upper left is a false colour view of the cloud top, the top right is a side view. Lower left shows simulated Infra Red radiation field with a mean optical thickness 50 (false colours), linear temperature gradient (from 300 to 220 K). The lower right is top view of the visible radiance, sun at 45°, (single scattering only, mean optical thickness$=$50). The statistics of the radiances are very close to those observed.

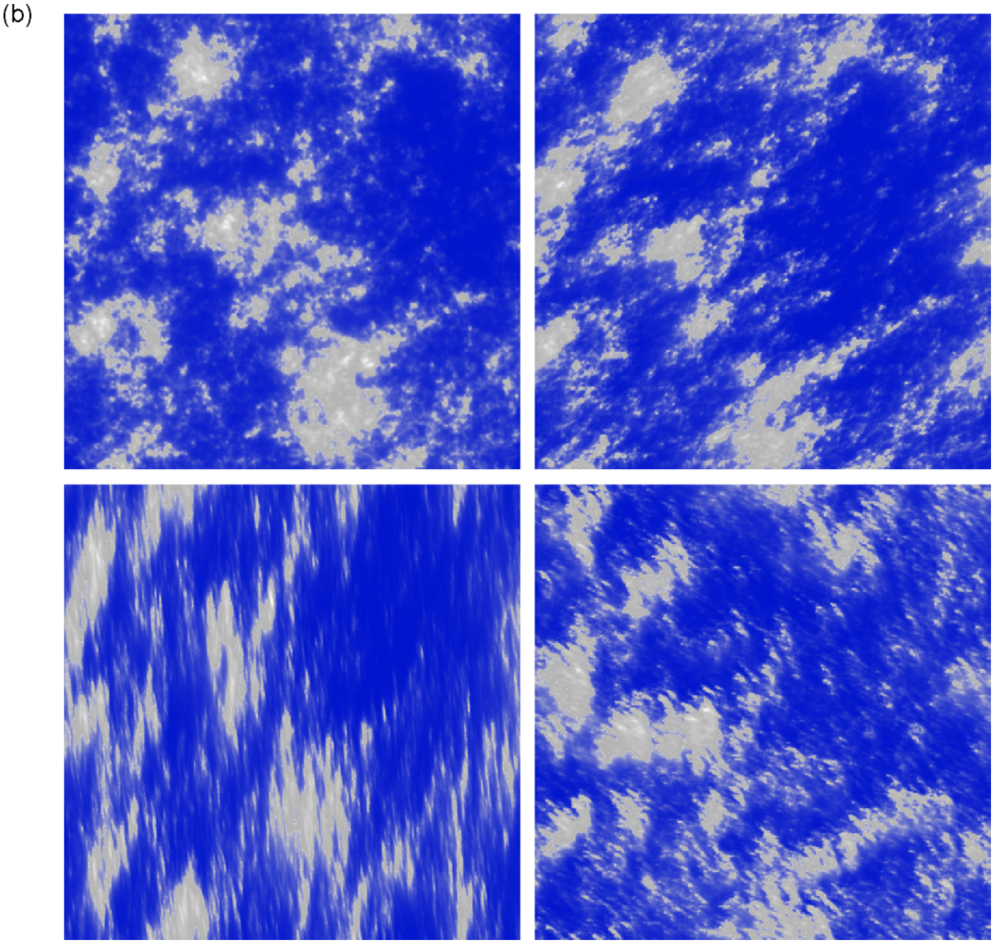

Fig. 5 (*continued*)

overall space–time scaling. In addition, the above assumes that the statistics are translationally invariant (i.e. the dynamical mechanisms are the same everywhere in space–time). T_λ is a scale changing operator; this, combined with a definition of the unit 'ball' (upon whose boundary lie all the unit vectors) defines the scale (λ) of all the vectors. Since, the system is scale invariant, T_λ must have group properties; in particular it is defined by an operator called a 'generator' G:

$$T_\lambda = \lambda^{-G} \tag{19}$$

T_λ is a generalized reduction by factor λ. When G is a matrix, then we have linear Generalized Scale Invariance (GSI).

With the aid of T_λ the extension of isotropic self-similar multifractals to realistic anisotropic modeling is conceptually straightforward, the vector norm $|\underline{X}|$ must be replaced by a 'scale function' satisfying $\|\lambda^{-G}\underline{X}\| = \lambda^{-1}\|\underline{X}\|$, and D by the 'elliptical dimension' = Trace G. Note that the scale function is not generally a metric. If G is the identity, then we recover isotropic (self-similar) multifractals (i.e.$\|\underline{X}\| \to |\underline{X}|$). In general G will be non-linear so that the anisotropy will depend not only on scale, but also on location.

The overall scaling of an anisotropic FIF field $R(\underline{X})$ is thus given by:

$$\Delta R(\underline{\Delta X}) = R(\underline{\Delta X} + \underline{X}) - R(\underline{X}),$$

$$\langle |\Delta R(T_\lambda \underline{\Delta X})|^q \rangle = \lambda^{-\xi(q)} \langle |\Delta R(\underline{\Delta X})|^q \rangle \tag{20}$$

where $\xi(q)$ is the scaling moment function.

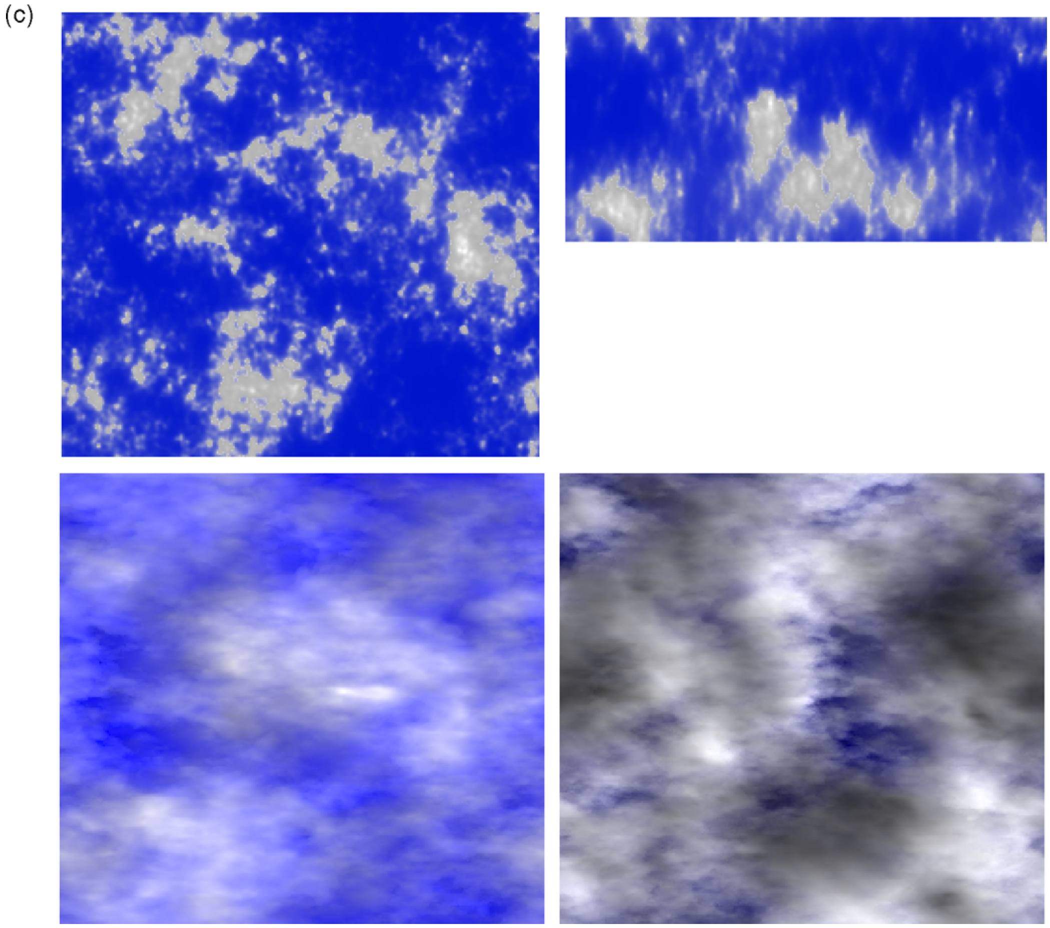

Fig. 5 (*continued*)

Finally, a comment is in order on space–time processes, where causality must be satisfied. Along a spatial axis, it is quite reasonable (although not in fact necessary) to assume left–right symmetry. On the contrary, along the time axis, there must be a complete asymmetry so that the future does not statistically influence the past. The appropriate additional conditions which are necessary in order to ensure that the future does not influence the past are given in (Marsan et al., 1996); we must use causal fractional integrations obtained by using Heaviside functions to cut-off the past in the Green's function in the fractional integral kernel (the powers of $||\underline{X}||$ in Eqs. (10) and (15)).

Although numerous numerical implementations of the above were made in the last 15 years, they suffered from certain problems of stability linked to the numerical approximation of the power law convolutions (fractional integrations). The key to stable numerics is to use appropriately (smoothly) truncated power laws: in 1D this can be achieved with 'Cauchy wavelets' (Schertzer et al., 2001). The non-trivial anisotropic extensions to higher dimensional spaces will be described in a forthcoming paper. See Fig. 5a–c for a comparison of anistropic and isotropic simulations showing how cloud and rain morphologies can change by changing the definition of scale. All the simulations will have very similar isotropic statistics. These simulations attempt to graphically show that different cloud types are—at least in principle—compatible with fixed values of α, C_1, H and how both infra red and visible radiances can

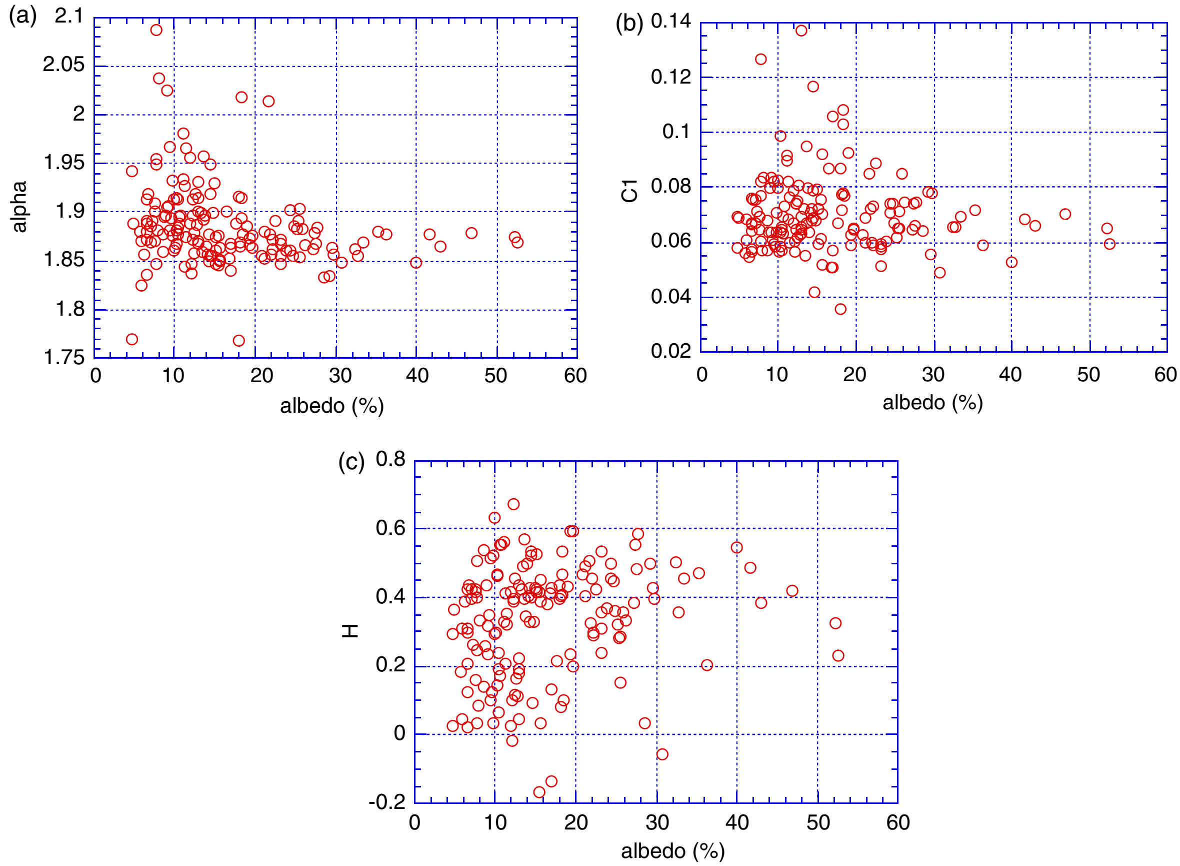

Fig. 6. AVHRR14: for 161 visible images. (a). (top left): scatterplot of α vs. average albedo estimated with cosine corrections as discussed in the text. The plot shows a wider scatter of α values for the low intensity images, with the value settling down to around 1.87 for the bright images. Note that values of $\alpha > 2$ are not theoretically possible, they are artifacts diue to inadequate statistics and/or small deviations from theory. (b). C_1 vs. albedo. Again, a wider scatter of C_1 values for low intensity images, with the values settling down to 0.07 for the brighter images. (c). H vs. albedo. The H values tend to be more highly variable and lower for the dimmer images. The higher albedo cases generally correspond to more cloud coverage, thicker clouds. Note that the H values of cloud-free land surfaces are typically small; the albedo being affected by the local topography gradients. This explains why the low albedo cases tend to have low H values.

be simulated from 3D stratified liquid water cloud density fields. Recently even more diversity and realism has been achieved using a wave-like fractional integration in Eq. (15).

4. Universal multiscaling

4.1. Isotropic multiscaling on an image by image basis

In Section 2, we showed—without yet quantifying it precisely—that cloud radiances had isotropic spectra that were accurately scaling; the spectrum is a second order statistic so that this characterizes a single value of the structure function: $\zeta(2)=\beta-1$ (Eq. (14)). In order to fully characterize the scaling, we need to characterize $\zeta(q)$; this is only practical with some parametric fit; following the arguments in Section 3.2, we shall therefore estimate C_1, α, H. Once again, before ensemble averaging, we first estimate the parameters on an image by image basis to see if there is are systematic variations, to examine the possibility that there might be several different ensembles present. The method we used was to first estimate a (scale by scale) conservative

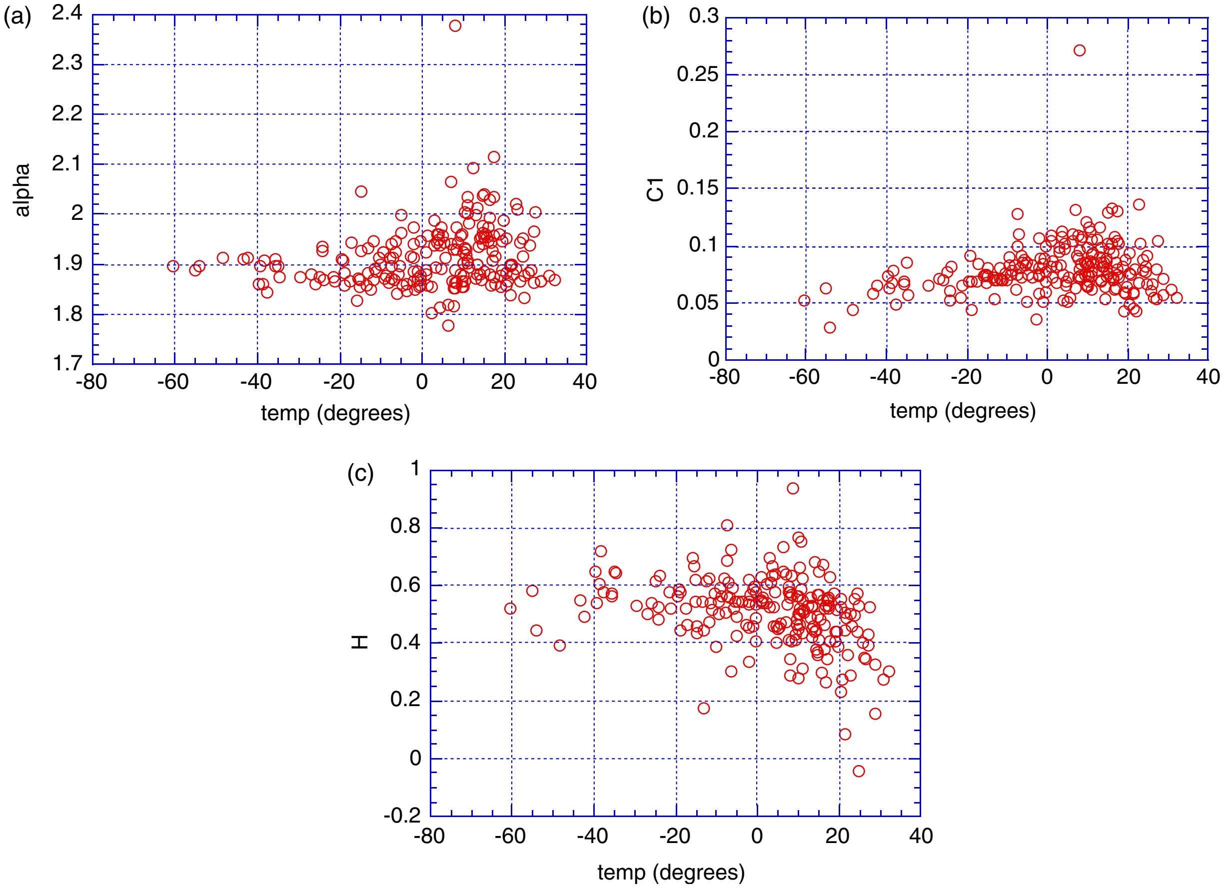

Fig. 7. 211 AVHRR12, Infra Red images as functions of the mean brightness temperature. The clouds with the higher tops are generally colder. (a) (top left): α The plot shows a wide scatter of alpha values for the warmer images. (b) (top right) C_1. There is a wide scatter of C_1 values for warmer images. (c) (bottom) H. The H values tend to be more highly variable and lower for the warmer images.

quantity analogous to the energy flux which we denote by ϕ. We then raise it to the η power, and systematically degrade its resolution (by averaging, ‘coarse graining’ or equivalently by using wavelets) to obtain $(\phi_\Lambda^\eta)_\lambda$. For each moment q, we can then perform a linear regression of $\log\langle(\phi_\Lambda^\eta)\rangle_\lambda$ against $\log\lambda$ to determine the slope $K(q,\eta)$ (Eq. (7)) and then from $K(q,\eta)$ we can perform a final log–log regression to determine α and $K(q,1)$ (and hence C_1) using Eq. (9); this is the DTM technique. Once α, C_1 are determined in this way, we can estimate the theoretical $K(2,1)$ (Eq. (6a)) and finally the last basic parameter H from the spectral exponent β (Eq. (14)).

The qualitative effects of varying the basic universal multifractal parameters can be described as follows. Visually, the effect of decreasing H is the increase the ‘roughness’ whereas C_1 varies the ‘sparseness (which increases with C_1). Finally, the tendency of the image to be dominated by holes increases as α is decreased. One way to get a better feel for this is via multifractal simulations; see the α, C_1, H space images in the multifractal explorer website (http://www.physics.mcgill.ca/~gang/multifrac/multifractals/isotropic.htm).

Fig. 6 shows a scatter plot for NOAA 14 visible channel (the NOAA 12 is very similar) of the parameters as functions of nominal albedo (estimated

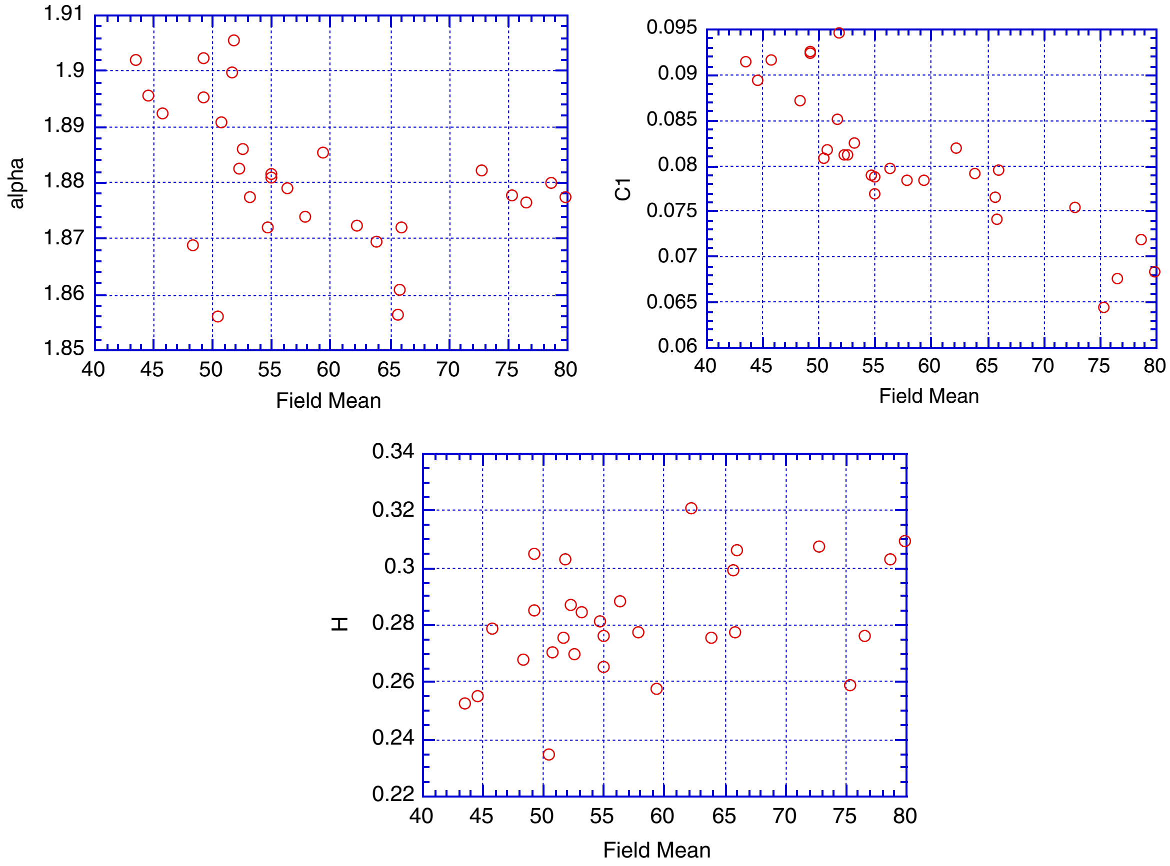

Fig. 8. (a) (top left): α vs. the mean visible brightness field (since sun and satellite angles did not vary much, no attempt at relative normalization was attempted; these are the mean of the raw radiances). The values of C_1 and α are plotted against each other for each of the 29 GMS used in the study. The α values are clustered in between 1.85 and 1.9 and the C_1 values around 0.07. (b) (top right) GMS visible, C_1 (c) (bottom) GMS images, H.

by using cosine corrections to sun and satellite angles as described in Section 2). We notice very little (if any) systematic dependence although the scatter is much higher for the low albedo cases which correspond to the low cloud cover images. Closer inspection shows that α, C_1 are still relatively stable and not far from the ensemble mean values (see below) whereas H varies considerably. This is in accord with results of radiative transfer on multifractal clouds (Naud et al., 1996; Schertzer et al., 1997) showing that radiation can be thought of as a (fractal) path integral through the cloud. This is effectively a fractional integration which therefore simply increases H without affecting α, C_1 in accord with this interpretation of Fig. 6. Indeed in situ (aircraft) measurements of cloud liquid water yield $\alpha=2$, $C_1=0.078$, $H=0.29$ (Lovejoy and Schertzer, 1995a; Davis et al., 1996) so that the α, C_1 values are indeed very similar. We also plotted the variation of parameters as functions of solar angle; this showed no systematic change. In Fig. 7 we turn to the infra red channel which we have plotted as functions of nominal temperature (deduced from the radiances by assuming perfect black body emission). With the exception of a single outlier for α, C_1, we again see that scatter in α, C_1 is fairly small although it increases with temperature (again corresponding to lower cloud cover since the ground is relatively warm compared to the cloud). In this case, the α, C_1 values are pretty close to those observed in the visible while

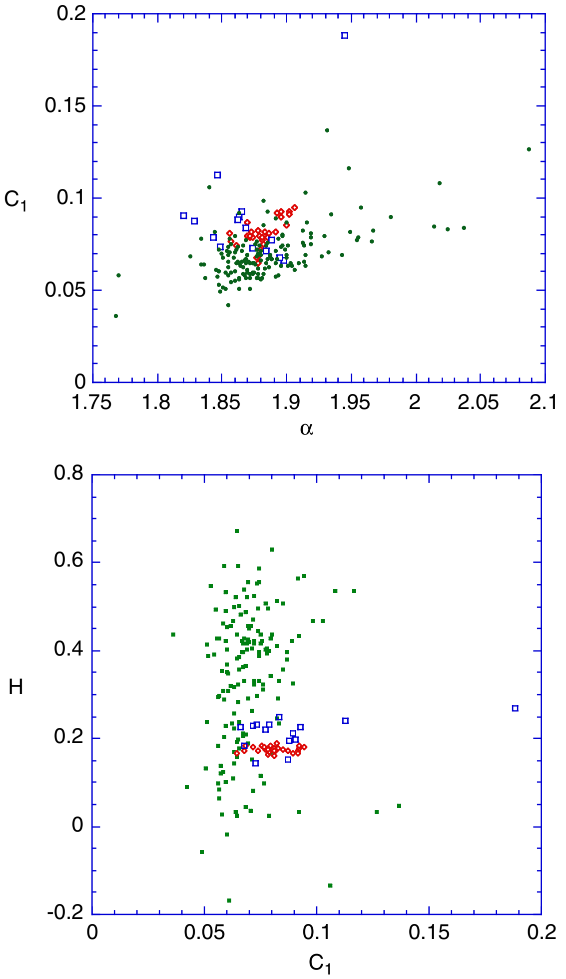

Fig. 9. (a).This shows a scatterplot intercomparison of visible data from GMS (red diamonds 10–5000 km, Pacific), AVHRR 14 (CART Oklahoma, small green squares, 1.1–280 km), AVHRR 9 (Atlantic Ocean, large blue squares, 1.1–280 km). (b). Same as 10a but for H, C_1.

the H values are a bit larger. Fig. 8 shows the corresponding results for the visible channel of the GMS. For all parameters we note a much lower GMS variability. This lower variability is to be expected if only because the GMS scales are larger (5000–10 km; λ is smaller) so that the cascade mechanism has had a smaller range over which to act. The fact that the data were all taken within a month also lead to a slightly lower variability as evidenced in the reduced effective outer scales discussed below. In addition, the background field (the Pacific ocean) is more homogenous than the AVHRR background which were taken over land (the Oklahoma ARM site). As deduced from the mean reflection, there is also a slight tendency for the C_1 values to decrease with cloudiness (note that for the GMS data satellite and sun angles were nearly the same for each image). Also note that the H values are systematically much lower than the AVHRR values which is consistent with the difference in background. The corresponding figure for the GMS IR channel is not shown since it is qualitatively similar to Fig. 8.

Finally, we show Fig. 9a which is an intercomparison of α, C_1 for various visible channels (and 9b for the corresponding the C_1, H scatter). On this figure we have also shown the results from 15 NOAA 9 visible scenes taken over the ocean off the coast of Florida analyzed in (Tessier et al., 1993). The method used in the latter paper did not carefully take into account the effect of spurious zero gradients so that the (reanalyzed) values here are somewhat different. This comparison is particularly interesting since the ocean (GMS, NOAA 9) data give results very close to each other for all parameters and close to the land (NOAA 14) values for α, C_1. The wide dispersion of H values for the land is thus presumably a consequence of seasonal land albedo changes (which include snow cover in some cases). Note that the cloud-free albedo is largely affected by local topography gradients so that the α, C_1 values are close to those of the topography (c.f. the values $\alpha = 1.78$, $C_1 = 0.12$, Gagnon et al., 2003). Since, for topography $H < 1$ (Gagnon et al., 2003 find that it is in the range $0.45 < H < 0.75$) the absolute gradient (i.e. a derivative of order $> H$) is approximately a conservative multi-fractal (with $H = 0$); this could explain the correlation of low albedo and low H in Fig. 6c.

4.2. The ensemble statistics

In the previous section we saw that the main difference between different images (and even wavelengths, satellites) was the H value; this was consistent with a simple radiative transfer model. We therefore only computed ensemble statistics for the conservative fluxes (which have $H = 0$) and small scatters in α, C_1 values. Before doing this we mention a technical point. The DTM method applies to conservative fields; we must therefore (fractionally) differentiate the radiances so that $H = 0$. The standard way is to use finite

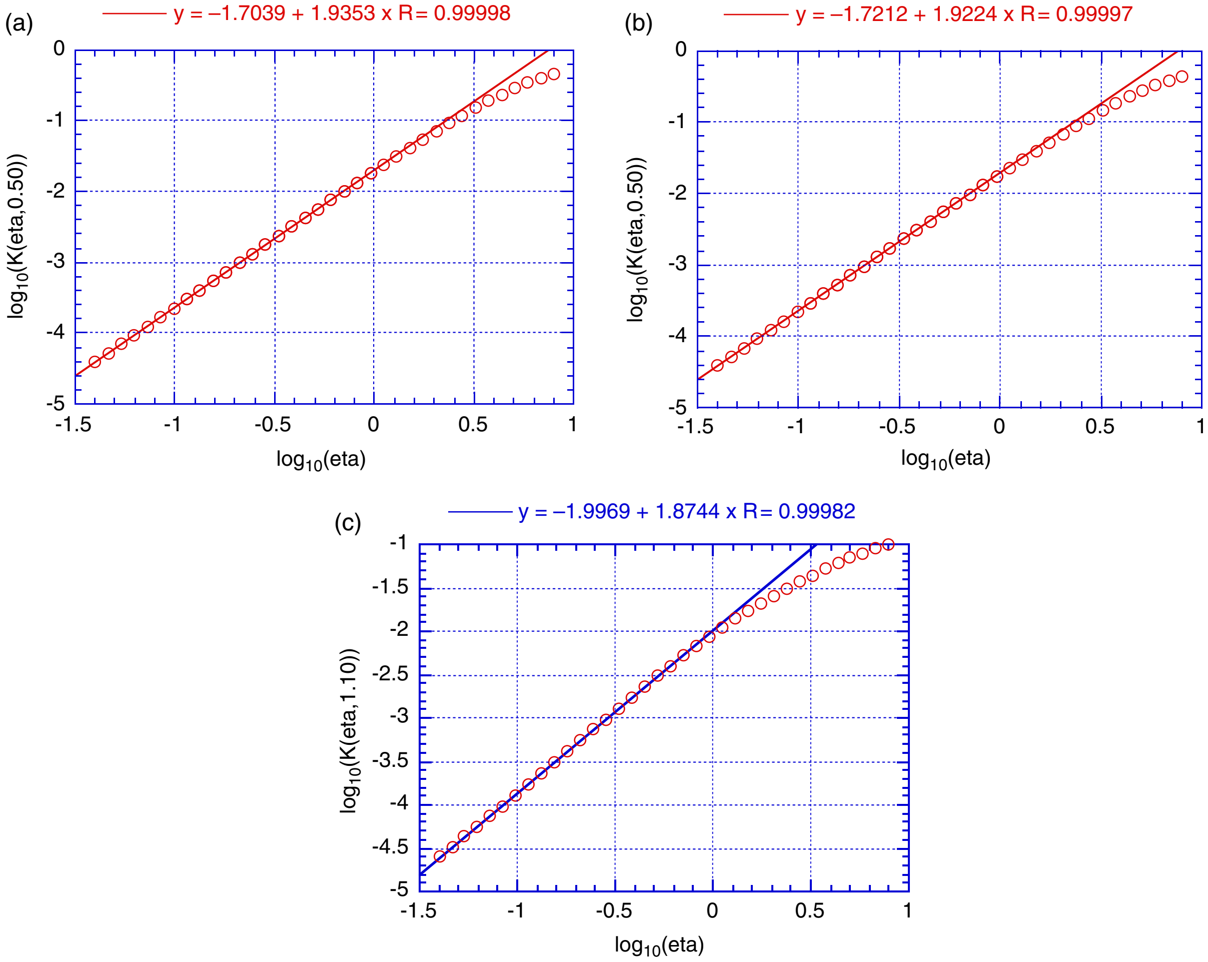

Fig. 10. DTM for visible imagery from each satellite for $q=0.5$. The deviations from the line at large η indicate multifractal phase transitions. (a) (top left): for AVHRR 12 visible images. (b) (top right): DTM for AVHRR 14 visible images The α values are clustered around 1.9 and the C_1 values in between 0.05 and 0.1. (c) (bottom left): GMS visible images.

difference approximations to the derivatives, either the finite difference Laplacian or the modulus of the gradient vector. In both cases, there is a problem that due to the low number of bits of dynamical range (e.g. 10 bits for the NOAA data), neighbouring pixels can be nominally identical so that we often obtain spurious zero gradients. While these will not greatly affect the large singularity, large q statistics, they give a large bias for the low q values which are critical for estimating α in the DTM technique. In order to avoid this problem, the data were first fractionally integrated by order $H=0.1$; the resulting fields were thus 32 bit and had essentially no spurious zero gradients. The absolute value of the finite difference Laplacian was then taken to obtain an estimate of ϕ. Fig. 10 shows the DTM results for $q=0.5$ for the visible channels of all three satellites. We see that up to a critical power η the scaling of the exponent is very good; this shows that universality is well obeyed; as expected at large enough η, the scaling breaks down (see below). Table 3a and b shows the overall inter-comparison of parameters. We see that the α values for all three satellites are roughly within the standard errors of the common value 1.93, whereas the C_1 values are a little different for visible (roughly 0.077) and IR (roughly 0.083). However, the H values are somewhat more

Table 3a

Intercomparison of the universal multifractal parameters; the errors are standard estimates obtained from the DTM ensemble regressions, not estimates of the 'spread' from one image to another

	NOAA-12 visible	NOAA-14 visible	GMS-5 visible	NOAA-12 Infra red	NOAA-14 Infra red	GMS-5 Infra red
α	1.935±.005	1.924±.003	1.88±0.05	1.937±.005	1.910±.003	1.86±.04
C_1	0.0780±.0005	0.0749±,0007	0.078±0.03	0.0826±,0002	0.079±.002	0.092±0.005
H	0.361±0.001	0.323±0.001	0.234±0.003	0.476±0.001	0.363±0.003	0.32±0.01

Table 3b

This is an intercomparison of various published universal multifractal parameters for visible channel cloud images

	Arneodo et al. (1999) and Arneodo et al. (1999)	Lewis et al. (2004)	Lewis et al. (2004)	Tessier et al. (1993))	GMS-5 visible	Sachs et al. (2002)	Lovejoy and Schertzer (1995a))
Description	A completely cloudy 15× 15 km section of marine LANDSAT data (30 m resolution), the data were assumed log normal.	12 LANDSAT scenes 28.5 m resolution (58.5×58.5 km), cloudy. A values in the range 1.5–2 gave about the same quality of regression (using structure functions.	13 LANDSAT scenes (58.5× 58.5 km) partly cloudy.	15 NOAA 9 marine images at 1.1 km resolution (512×512 pixel images). The data were reanalyzed here (Fig. 10) after eliminating spurious zero gradients (see text).	From Table 2a.	38 ground photographs (looking up), resolution roughly 1 m, 1000–2000 pixels in size.	Aircraft cloud liquid water density (10 m resolution)
α	2	2	1.37	1.87	1.88	1.77	2
C_1	0.035	0.029	0.089	0.081	0.078	0.061	0.078
H	0.38	0.354	0.18	0.22	0.234	0.61	0.29

Note that only the H value seems sensitive to the difference between land, ocean and sky backgrounds (AVHRR, GMS, respectively), see also Fig. 10. The far right column compares this to in situ liquid water content; the α, C_1 values are very close to the radiative values as expected by simple arguments about radiative transfer.

variable—as expected from our image by image analysis.

The values are close to those found in infra red and visible in (Tessier et al., 1993), (see Fig. 10 for a reanalysis of the visible data using the above technique for avoiding spurious zeroes). Other comparable visible studies spanning the range 1 m–550 km are compared in Table 3b. Only the H value seemed sensitive to the differences in the background (land, ocean or sky) while being quite constant (roughly 0.2) for all the marine data except for those small scale scenes deliberately selected to be mostly ‘cloudy’ (these were close to the ensemble mean NOAA 12, 14 values over land).

The breakdown of linear behaviour of log K $(2,\eta)$ at large η occurs because Eq. (9) is only valid for ‘bare’ ensemble moments. We have already mentioned that it breaks down for $q>q_D$ due to the divergence of the ‘dressed’ moments. For finite samples, it will also breakdown since there will be a finite maximum order of singularity γ_s; according to the Legendre result (Eq. (3)) this will yield a linear $K(q)$ whose slope$=\gamma_s$ (Schertzer and Lovejoy, 1992). This is investigated in more detail in Stanway (2000) and Lovejoy et al. (2001); we find that for the visible data there is only a second order transition, whereas for the infra red data, there is a first order transition (divergence of moments) at $q_D=1.9$.

We now consider the quality of the multiscaling, with respect to a series of more and more demanding hypotheses. Since, the four AVHRR data sets had very similar statistical behaviours, let us illustrate this using the AVHRR14 IR set (see Fig. 11). First, consider the least demanding multiscaling hypothesis: that for each moment, we have a pure unconstrained power law, i.e. we fit the best straight line on a log–log plot. This leads to an overall (average over all moments up to $q=1.6$ and all scales) standard deviation of residues (of the $\log_{10}$ moments) of $\sigma_{\mathrm{res}}=\pm 0.0012$, i.e. a $\pm 0.28\%$ deviation. This is considered further in Section 4.3. If alternatively, we constrain the fit by imposing the external scale of 20,000 km for all the moments, we obtain the dashed lines in Fig. 11 with a corresponding $\sigma_{\mathrm{res}}=\pm 0.0022$ $(=\pm 0.51\%)$. Finally, we can consider theoretical lines with slopes theoretically determined by the ensemble universal multifractal parameters $C_1=0.079$, $\alpha=1.91$ and by the constraint that they pass through the origin (corresponding to an outer scale of 20,000 km). In this case, we obtain $\sigma_{\mathrm{res}}=\pm 0.012$ $(=\pm 2.8\%)$. If we consider only the first two cases (i.e. multiscaling without the universality constraint), then the residuals are so small that no systematic deviation of scaling can be detected above random fluctuations. However, we shall see in Section 4.4 that in the case of universal multifractals (with 5–10 times larger residuals) much of the deviations from pure (isotropic) universal multifractal power law scaling can in fact be accounted for by nonpower law ‘subscaling’ corrections; in fact a single extra subscaling parameter reduces the standard deviation of the residues to $\sigma_{\mathrm{res}}=\pm 0.0025$ $(=\pm 0.58\%)$ so that theoretical universal multifractals with a single extra subscaling exponent yields residuals comparable to the dashed lines in Fig. 11.

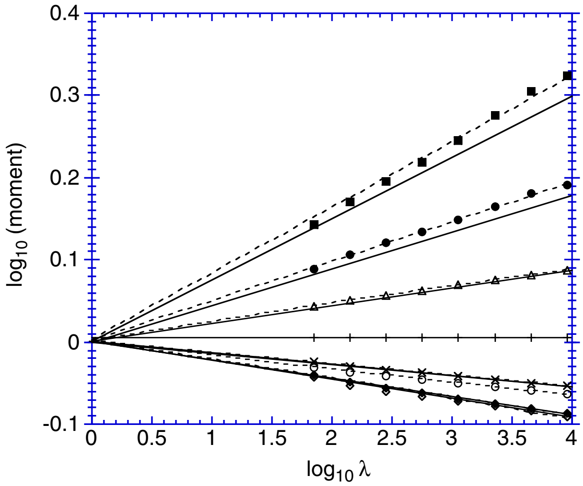

Fig. 11. $\lambda=L/L_{\mathrm{eff}}$ with $L_{\mathrm{eff}}=20{,}000$ km for the NOAA 14 IR data, moments $q=0.2$, 0.4,…,1.6. The solid lines shown are the theoretical lines with $C_1=0.079$, $\alpha=1.91$, (using Eqs. (6) and (9)) the dashed lines are the best linear regressions. All lines were forced to go through the external scale (the origin here). If this constraint is dropped, the regression lines are quite close to the dashed lines but do not quite go through the origin; the intersection points with the horizontal axis are given in Table 4.

Fig. 11 and others like it for the other channels and satellites, were obtained with a fairly simple isotropic analysis technique using a large quantity of the data and lead to remarkable agreement with the predictions of cascade theories. This agreement includes the existence of multifractal universality classes and multifractal phase transitions which are discussed in Stanway (2000) and Lovejoy et al. (2001). But how is it possible for the diverse morphology of atmospheric structures to be compatible with wide range scaling? We have already attempted to answer this with the help of anisotropic simulations in Section 3: although each having different morphologies/textures they would all give nearly the same isotropic exponents. More generally, we must consider the two parts of a scaling system, each of which corresponds to a (mathematical) group and generator. The first characterizes the statistics, the second defines the scale changing operator and hence the notion of scale itself. The statistical moments shown in Fig. 11 are thus only half the picture. Implicit in the figure is the use of the naïve Euclidean notion of scale, i.e. standard distances and standard isotropic scale changes. The analyses are isotropic since in order to estimate the data at lower and lower resolutions, averaging was performed over squares whose shape was independent of scale (large and small squares are related by a $T_\lambda = \lambda^{-G}$ with G, dentity, see Section 3). These isotropic analyses ‘wash out’ all but the strongest anisotropies. On the contrary, the general formalism for scale invariance discussed in Section 3 shows that very general anisotropies/morphologies are compatible with the scaling in Fig. 11.

4.3. The cascade model and the outer scale

Up until now, we have only considered the scaling exponents—the slopes on the log moment vs. log scale plots, we have not considered the question of the outer scale of the multiscaling regime. The ‘effective outer scale’ L_{eff} is where a cascade must start in order to be able to generate the observed variability and requires study of the intercepts. To see this, recall:

$$\langle \phi_\lambda^q \rangle = \lambda^{K(q)}; \qquad \lambda = \frac{L_{\text{eff}}}{l} \tag{21}$$

when $L = L_{\text{eff}}$, we have $\lambda = 1$ and $\langle \varepsilon_1^q \rangle = 1$ implying that ε_1 is a ‘sure’ (nonrandom) value; L_{eff} is therefore the outer scale of a scale invariant (unbounded) cascade which would yield all the observed variability (see Fig. 12 for a schematic). Since, the true cascade process has variable input flux at the largest scale, not all the variability is due to the cascade hence if a true (infinite) ensemble were used to estimate the moments, L_{eff} would be an upper bound on the outer scale here however the finiteness of the ensemble tends to counter this, it lowers L_{eff}.

Using a linear regression of $\log\langle \phi_\lambda^q \rangle$ against $\log L/L_{\text{eff}}$, (i.e. without constraining the lines to pass through the origin in Fig. 11), $\log L_{\text{eff}}$ can be estimated from the intercept of the regression line (the extrapolated value of $\log L_{\text{eff}}$ such that $\log\langle \phi_\lambda^q \rangle = 0$). The results for various statistical moments and satellites and channels are shown in Table 4 which show that for the NOAA data, the lines for the different moments point quite accurately to the same outer scale L_{eff}. Indeed, for the NOAA data sets, L_{eff} is very close to the largest great circle distance (20,000 km).

By considering the means for each satellite over the different moments (q values), we see that even when extrapolating over nearly a factor of 100 (20,000/280 km) in scale that the mean $\log_{10}(L_{\text{eff}}/L_{\text{ref}}) = 0.015 \pm 0.06$ corresponding to $L_{\text{eff}} \approx 20{,}700 \pm 3{,}000$ km (this is the exponential of the mean; the mean of the exponentials gives a very similar result). The limited GMS-5 sampling leads to an underestimate of the ensemble variability so that the GMS-5 data have a lower mean $L_{\text{eff}}: \log_{10}(L_{\text{eff}}/20{,}000\ \text{km}) = -0.63 \pm 0.13$, i.e. $L_{\text{eff}} \approx 4700 \pm 1500$ km. Although this difference of factor $\lambda' = 20{,}700/4700 = 4.4$ may seem large, it actually implies only a very small underestimate of the variability by the GMS-5 data: for example, since we find $K(2) = 0.16$, we see that if the standard deviations were increased by a factor of only $\lambda'^{K(2)/2} = 1.1$ then the two L_{eff} estimates would agree. Note that this direct confirmation of Eq. (2) on the GMS data shows that 4700 km is a lower bound on the true outer scale.

4.4. Quantifying the deviations of the average isotropic statistics from universal multifractal scaling

Although the scaling with outer scale $L_{\text{eff}} = 20{,}000$ km fits quite well, we shall quantify this statement. We have mentioned that the residues to scaling with unconstrained slopes were of

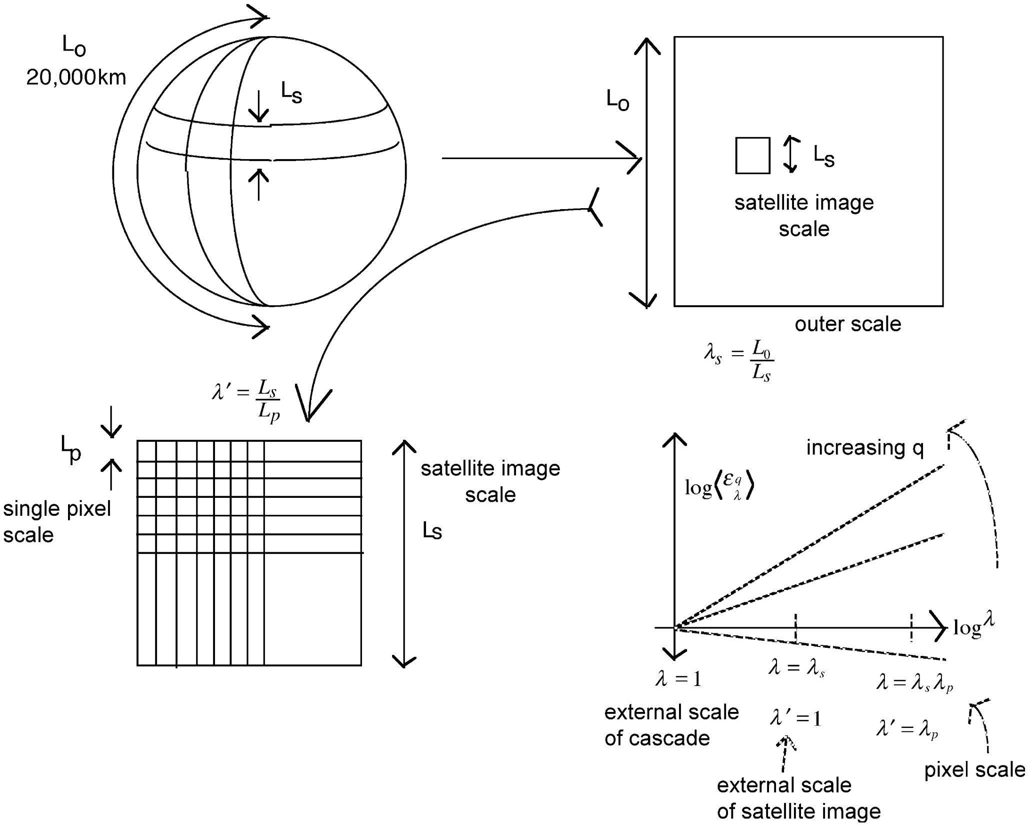

Fig. 12. Cascade outer scale estimation from climatological ensemble. At the top left, the limited area satellite data sets are shown at scale L_s; this is substantially smaller than the planetary scale L_0. Top left; the same except with a flat earth in order to clearly show the scales, the scale ratio $L_0/L_s = \lambda_s$. On the bottom left, we see that within each satellite picture there are resolution elements of scale L_p so that over the satellite image we have another ratio $L_s/L_p = \lambda'$. The overall scale ratio from the planetary scale to a pixel is $\lambda = \lambda' \lambda_s$. Since, the moments factorize: $\langle \varepsilon^q_{\lambda_s \lambda'} \rangle = \lambda_s^{K(q)} \lambda' K(q)$ we see that a plot of $\log\langle \varepsilon^q_\lambda \rangle$ vs. $\log \lambda'$ will cross the axis at the outer scale (bottom right).

Table 4
The numbers are $\log_{10} L_{\rm eff}/L_{\rm ref}$, where $L_{\rm eff}$ is the scale ratio of the scale where the variability disappears (where the extrapolated lines in Fig. 12 cross below the horizontal axis) and $L_{\rm eff} = 20{,}000$ km is the reference scale (taken as the largest great circle distance on the earth)

q	NOAA12 vis	NOAA12 IR	NOAA14 vis	NOAA14 IR	GMS vis	GMS IR
Number of pictures	134	354	153	214	29	29
0.2	0.13	0.34	0.18	0.34	−0.77	−0.52
0.4	0.08	0.30	0.10	0.24	−0.76	−0.51
0.6	0.02	0.22	0.02	0.12	−0.76	−0.48
0.8	−0.01	0.07	0.00	−0.10	−0.76	−0.51
1.2	−0.07	−0.14	−0.14	0.29	−0.75	−0.49
1.4	−0.10	−0.27	−0.18	0.02	−0.75	−0.49
1.6	−0.12	−0.51	−0.22	−0.23	−0.74	−0.50
Average	−0.01	0.00	−0.03	0.10	−0.76	−0.50

Moments higher than 1.6, where not used due to 1st and 2nd order multifractal phase transitions in the IR, vis. data, respectively. Note that for the NOAA data, the mean of the means is 0.015 corresponding to an outer scale of $L_{\rm eff} = 20{,}700$ km. The mean of the GMS data is −0.63 corresponding to $L_{\rm eff} = 4700$ km, but the data are from a single month therefore underestimate the climatological variability.

the order $\sigma_{\mathrm{res}} = \pm 0.002$ which is so small that systematic deviations could not be established above random fluctuations. However, if we consider residues with respect to universal multifractal scaling, then $\sigma_{\mathrm{res}} = \pm 0.02$ which is large enough to show some systematic deviation.

In order to study these small deviations, we may consider the following perturbed scaling behavior:

$$\langle \phi_\lambda^q \rangle \approx \lambda^{K(q,\lambda,\Lambda)}; \quad 1 \le \lambda \le \Lambda,$$

$$K(q,\lambda,\Lambda) = K(q)\left(1 - \left(\frac{w}{2}\right)\left(\frac{\log \lambda}{\log \Lambda}\right)\right) \tag{22}$$

where the constant $w/2$, may be obtained by a second order regression of $\mathrm{Log}\langle \phi_\lambda^q \rangle$ vs. $\mathrm{Log}\,\lambda$ and Λ is the total range of scales over which the cascade develops (e.g. planetary scales to dissipation scales yields $\Lambda \approx 10^{10}$). This may be considered as simply the first two terms in an infinite series of corrections. Such a series could arise either from scaling (log(log) corrections; see below), or from nonscaling corrections. An example of the latter is given by the continuous in scale limit of a discrete cascade model in which the singularities are attenuated algebraically at each step (see the moment exponent in Table 2b).

Whatever its origin, it can be quantified by defining the ratio of the quadratic term by the linear term of the second order regression (Eq. (20)):

$$\delta_e = w/(2\,\mathrm{Log}\,\Lambda) \tag{23a}$$

which is the relative linear deviation of $\mathrm{Log}\langle \phi_\lambda^q \rangle = K(q,\lambda,\Lambda)\mathrm{Log}\,\lambda$ with respect to its linear trend $K(q)\log\lambda$ per factor factor e in scale. It is perhaps more convenient to consider the corresponding relative linear deviation δ_2 per octave:

$$\delta_2 = \delta_e\,\mathrm{Log}\,2 \tag{23b}$$

The second order regressions yield the following empirical estimates of δ_2 (Table 5).

Before interpreting these values further, it should be stressed that these small quadratic terms result from a combination of random fluctuations and small systematic deviations; they are thus upper bounds on true deviations from universal mulifractality per octave in scale. With this in mind, taking the mean δ_2 of the values in Table 5 we obtain $\delta_2 \approx 0.016$, using this figure we can estimate the upper bound of the cumulative effect over 30 octaves ($10^9 \approx$ planetary scale/dissipation scale) is a factor of 0.33. We could note that in two of the six cases the sign is negative implying that the cascade becomes a little more violent—not less—at smaller scales (although for both negative cases, the values are very small). In any case, it is interesting to compare these results with those of (Sachs et al., 2002) (Table 2b) who found at scales of 1 m–1 km (a factor of about 1000 smaller than the AVHRR), that $\alpha \approx 1.77$, $C_1 \approx 0.061$ so that α was very close to those measured here and C_1 had only decreased by about 0.078–0.061. Analysis shows that this implies a more stringent bound on the amplitude of systematic effects; $\delta_2 < 0.011$. Note that (Sachs et al., 2002) used ground based photography and looked up at the sky obtaining a somewhat higher value of $H = 0.61$.

We now consider the possibility that deviations from pure power law and universal multifractal behaviour are nevertheless scale invariant (we do not consider here variations due to anisotropy which in principle could be larger). To understand this, recall

Table 5

Estimates of the relative linear deviation δ_2 per octave (Eqs. (22)–(24)) obtained by second order regression of $\mathrm{Log}\langle \phi_\lambda^q \rangle$ vs. $\mathrm{Log}\,\lambda$, for each q the δ_2 is directly determined from the ratio of the quadratic to linear terms, using the theoretical universal $K(q)$ with C_1 and α as in Table 3a

	NOAA12 vis	NOAA12 IR	NOAA14 vis	NOAA14 IR	GMS vis	GMS IR
No. of pictures	134	354	153	214	29	29
δ_2	0.016	0.045	-0.008	0.033	0.014	-0.0042
Correction factor (per 10^3)	0.7	2.8	1.2	2.1	0.7	1.1

The values quoted are the means over the moments $q = 0.2, 0.4, \ldots, 1.6$. Since, these values are simply derived from the small quadratic terms, they are due to a combination of some systematic effects and some random fluctuations; they are hence upper bounds on any real systematic deviation from multifractal universality. The outer scale for the AVHRR data was taken as 20,000 km, for the GMS, due to the smaller sample size it was taken as 4700 km (see text).

that the usual discrete in scale multiplicative cascade obeys Eq. (2) exactly, variations in the details of the cascade could introduce slowly varying corrections. Indeed, these cascades have been specifically designed so that the moments have exact power law scaling. However, power laws are not the only functions which are scale free; logarithms and iterated logarithms are also scaling so that if scaling is the only a priori restriction we place on our process, we may anticipate empirical scaling fields to have statistics of the form:

$$\langle \varepsilon_\lambda^q \rangle = \lambda^{K(q)}(1+\log(\lambda))^{\Delta_1(q)}(1+\log(1+\log\lambda))^{\Delta_2(q)}, \ldots \qquad (24)$$

where the Δ's are 'sub' scaling exponents (the '1's' are included so that the limit $\lambda \to 1$ is correct; in the small scale, large λ limit they are negligible). These subscaling behaviors could arise because—like power laws—the iterated logarithm functions are also scale invariant.

To test this possibility, we now can consider scaling and log (but not log–log) corrections:

$$\log(\lambda^{-(C_1/\alpha-1)(q^\alpha-q)}\langle \varphi_\lambda^q \rangle) = \Delta_1(q)\log(1+\log\lambda) \qquad (25)$$

i.e. by plotting the residuals of power law scaling against log(log λ) we can estimate $\Delta(q)$ and determine how well the subscaling quantifies the deviations. Note that to be consistent, we should use $\lambda = L/L_{\mathrm{eff}}$ with $L_{\mathrm{eff}} = 20{,}000$ km as argued above. In addition, note that the residuals are determined with respect to the universal form for $K(q)$ (they are the difference between the data and the lines in Fig. 11) so that for all moments and scales they are determined by just two regression parameters. Fig. 13 shows the comparison for the NOAA 14 Infra Red data, showing that the subscaling is reasonable. This can be quantified either with respect to an arbitrary $\Delta(q)$ function (as in the figure), or with respect to a theoretical $\Delta(q)$. From the figure, we can see that an arbitrary $\Delta_1(q)$ can explain the moments up to $q = 1.4$ to within an error of $\sigma_{\mathrm{res}} = \pm 0.0025$ $(= \pm 0.58\%)$. If we take $\Delta_1(q) = (C_\Delta/(\alpha-1))(q^\alpha - q)$ we can see that the form Eq. (25) can be expanded as a series of the form Eq. (22) if $C_\Delta = C_1 w/\log \Lambda$. From regression, we find that $C_\Delta = 0.040$ yields a fit to within $\sigma_{\mathrm{res}} \pm 0.0035$ $(= \pm 0.81\%)$ implying that $w/\log \Lambda \approx 0.040/0.079 = 0.51$. In summary, using three parameters α, C_1, C_Δ with L_{eff} taken as the size of the planet (i.e. not fit), we can explain the observed moments up to order $q = 1.6$ to with an error of $\log_{10}$ (moment) $= \pm 0.0035$ $(= \pm 0.81\%)$. The results for the other AVHRR data are quantitatively similar.

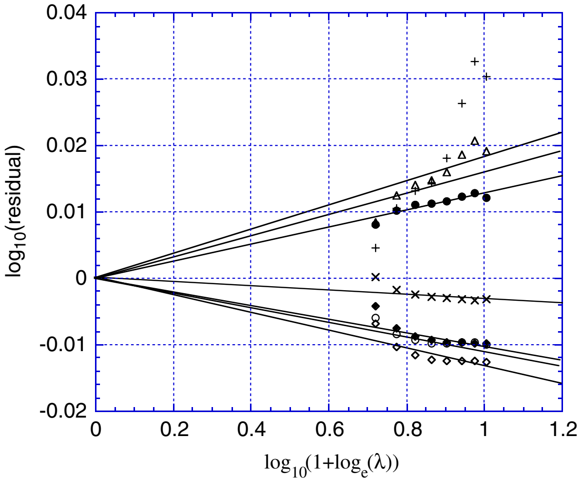

Fig. 13. NOAA 14 IR residuals for theory with $C_1 = 0.079$, $\alpha = 1.91$. The lines are regressions; from top to bottom they correspond to $q = 1.6$, 1.4,…0.4, 0.2.

4.5. The global significance of our results

We have used data from Oklahoma, the Atlantic Ocean near Florida and the central Pacific ocean in order to make broad quantitative conclusions about the spatial variability of atmospheric dynamics. The basic reason that we have confidence in the generality of our exponent estimates is because they are of a sufficiently fundamental nature that they are unlikely to be affected by purely local conditions. For example, one is used to the idea that in turbulent wind fields, the Kolmogorov exponent 1/3 is the same in vastly different climatological regimes (it has even been observed in Jupiter, and in intergalactic jets). Indeed, the main reason for suspecting genuine variation is that we observe radiation fields which are determined not only by the properties of the turbulent cloud fields, but also by the variability of the underlying background (e.g. ocean or land surface, or when looking up, the sky). Since, we argued that the latter mostly affects H, this explains the robustness of the α, C_1 estimates.

5. Conclusions

There is a growing consensus that precipitation and other atmospheric fields are scaling (they have scale invariant generators/exponents)—at least over limited ranges. Unfortunately, it is very difficult to measure space–time rainfall; surrogates are usually used instead. For example, radar does have good spatio-temporal resolution but the interpretation of the microwave backscatter in terms of rain itself requires various hypotheses about the sub pulse scale. Rain gauges do measure point rainfall but kriging and other techniques for obtaining spatial rainfall involve their own scaling (trivial or otherwise) assumptions. In addition, the gauges have severe problems measuring low rain rates, a problem whose importance has been underestimated but which can indeed lead to spurious breaks in the scaling. Visible and infra red satellite data have also been used to estimate rain; this data has the advantage of potentially covering huge scale ranges. Due to these and other difficulties, caused by the extreme intermittency/variability over huge scale ranges, it seems inevitable that multifractal models will be required for modeling rain and the corresponding visible, infra red or microwave fields. In the case of rain gauges, they will be necessary to model the effect of small scale variability and low rain rates.

Before directly tackling this problem it is necessary to determine the scaling ranges and types as well as to consider plausible models. The usual satellite rain surrogates are obtained by judiciously combining visible, infra red, passive microwave or other data sets at various resolutions. Rather than study the complex scale dependence of these surrogates, we directly examine the scaling of the visible and infra red radiances, using (primarily) 909 satellite images from three satellites and six sensors. The idea is to exploit the fact that scale invariance is a symmetry principle and that the cloud density, cloud radiances and rain fields are all strongly non-linearly coupled. This means that although clearly the cloud radiances cannot be directly interpreted in terms of rain, that nevertheless that a break in the scaling in any of the radiances will likely show up in the others as well as in rain (even if the exact type of scaling is not expected to be the same). In Section 2 we considered the familiar (isotropic) spectra directly indicating scaling of cloud radiances over the range 5000–1 km (down to 1 m if we take into account ground based photography). Since, the spectrum is a second order moment (whose is exponent is simply one of an infinite multifractal hierarchy), this justifies the consideration of detailed multifractal models; we concentrated on those with the most physical justification: the (strong) universal Log-Levy model showing how these can be extended to nonconservative multifractals by fractional integration. We also gave a quick overview of various multifractal models pointing out their limitations; only the Fractionally Integrated Flux model featured both continuous in scale generators and unbounded singularities which are required for realism. We gave examples of cloud, and rain fields comparing isotropic (self-similar) and anisotropic cases showing how these processes can be used for simulating visible, infra red satellite imagery which are the basis of satellite rain algorithms such as RAINSAT.

We then considered the multiscaling of the radiances; first on an image by image basis. We showed that for α, C_1, there were no clear trends with albedo, sun angle, mean cloud temperature or wavelength with values for a narrowly varying around 1.9, and C_1 mostly between 0.03 and 0.15 concentrated near 0.08. However, the H values did have a tendency to increase with cloud cover (as estimated by albedo) and were also sensitive to the background (ocean, land or sky). This is in rough accord with simple radiative transfer arguments to the effect that in the visible the photons effectively fractionally integrate the liquid water field changing H but not α, C_1.

Finally, we considered the multiscaling of the ensemble radiance statistics. We showed how a climatologically significant sample could be used to estimate the effective outer scale of the cascade. When we did this, we found values very consistent between satellites and sensors varying with little scatter around 20,000 km, the largest great circle distance on the earth. This is direct evidence that the cloud dynamics could be explained by planetary scale cascade processes. In addition, we showed that the standard deviation of residues from pure power law behaviour were in the range ± 0.3–0.5%; the upper bound on the possible systematic deviations from the more restrictive, theoretical universal multifractal behaviour were 1–2%/octave in scale. We then considered the hypothesis that the deviations from pure universal multifractal cascade starting at exactly 20,000 km could be explained as 'sub power law' (logarithmic) but still scaling corrections. We showed that we only three parameters (two for the power law, one for the corrections), we could account for the moments to within ±0.8%.

References

Anselmet, F., Antonia, R.A., Danaila, L., 2001. Turbulent flows and intermittency in laboratory experiments. Plan. Space Sci. 49, 1177–1191.

Arneodo, A., Decoster, N., Roux, S.G., 1999. Intermittency, Log-normal statistics, and multifractal cascade process in high-resolution satellite images of cloud structure. Phys. Rev. Lett. 83, 1255–1258.

Barnsley, M.F., 1993. Fractals Everywhere. Academic Press, Boston.

Basu, S., Foufoula-Georgiou, E., Porté-Agel, F. Synthtic turbulence, fractal interpolation and large-eddy simulations, Phys. Rev. Lett.

Bell, T.L., 1987. A space–time stochastic model of rainfall for satellite remote sensing studies. Geophys. Res. 92, 9631–9644.

Bellon, A., Lovejoy, S., Austin, G.L., 1980. A short term precipitation forecasting procedure using combined radar and satellite data. Mon. Wea. Rev. 108, 1554–1566.

Bendjoudi, H., Hubert, P., Schertzer, D., Lovejoy, S., 1997. Interprétation multifractale des courbes intensité-durée-fréquence des precipitations, Multifractal point of view on rainfall intensity-duration-frequency curves. C.R.A.S., Sciences de la terre et des planetes/Earth and Planetary Sciences 325, 323–326.

Burlando, P., Rosso, R., 1996. Scaling and multiscaling models of depth-duration frequency curves for storm precipitation. J. Hydrol. 187, 45–64.

Cahalan, R., 1994. Bounded cascade clouds: albedo and effective thickness. Nonlin. Proc. Geophys. 1, 156–167.

Chigirinskaya, Y., Hubert, P., Bendjoudi, H., Schertzer, D., Lovejoy, S., 2002. Multifractal modelling of river runoff and seasonal periodicity, PFHD International Conference, Timisoara, Romania 2002 pp. 43–46.

Davis, A., Marshak, A., Wiscombe, W., Cahalan, R., 1996. Scale Invariance of liquid water distributions in Marine Stratocumulus. Part I: Spectral properties and stationarity issues. J. Atmos. Sci. 53, 1538–1558.

Deidda, R., 2000. Rainfall downscaling in a space–time multifractal framework. Water Resources Res. 36, 1779–1794.

De Lima, I., Multifractals and the temporal structure of rainfall, PhD Thesis, Wageningen, 1998.

De Lima, I., Schertzer, D., Lovejoy, S., de Lima, J. Multifractals and the study of extreme precipitation events: a case study from semi-arid and humid regions in Portugal, in Conference on Water Resources Management in Arid Regions, Kuwait, 2001.

De Lima, I., Schertzer, D., Lovejoy, S. De Lima, J.L.M.P., Coelho, M.F.E.S. Multifractal tools applied to the study of precipitation extremes, in EWRA Symposium on Water resources management: risks and challenges for the 21st century, Izmir, Turkey, 2004.

Desaulniers-Soucy, N., Empirical Test of the multifractal continuum limit in rain, PhD thesis, McGill, Montreal, 1999.

Duncan, M.R., The universal multifractal nature of radar echo fluctuations, PhD. thesis, McGill, Montreal, 1993.

Fabry, F., 1996. On the determination of scale ranges for precipitation fields. J. Geophys. Res. D101, 12819–12826.

Fournier, A., Fussel, D., Carpenter, L., 1982. Computer rendering of stochastic models. Commun. ACM 6, 371–374.

Fraedrich, K., Larnder, C., 1993. Scaling regimes of composite rainfall time series. Tellus 45, 289–298.

Gagnon, J.S., Lovejoy, S., Schertzer, D., 2003. Multifractal surfaces and topography. Europhys. Lett. 62, 801–807.

Gaonac'h, H., Lovejoy, S., Schertzer, D. (submitted) Multifractal analysis of infrared imagery of active thermal features at Kilauea volcano, J. Geophys. Res., (7/99).

Gupta, V.K., Waymire, E., 1990. Multiscaling properties of spatial rainfall and river distribution. J. Geophys. Res. 95 (D3), 1999–2010.

Gupta, V.K., Waymire, E., 1993. A statistica l analysis of mesoscale rainfall as a random cascade. J. Appl. Meteorol. 32, 251–267.

Harris, D., Menabde, M., Seed, A., Austin, G., 1996. Multifractal characterizastion of rain fields with a strong orographics influence. J. Geophys. Res. 101, 26405–26414.

Hubert, P., Tessier, Y., Ladoy, P., Lovejoy, S., Schertzer, D., Carbonnel, J.P., Violette, S., Desurosne, I., Schmitt, F., 1993. Multifractals and extreme rainfall events. Geophys. Res. Lett. 20 (10), 931–934.

Hubert, P., Bendjoudi, H., Schertzer, D., Lovejoy, S., 1995. Fractals et mulitfractals appliqués à l'étude de la varaibilité temporelle des précipitations. In: Feddes, R.A. (Ed.), Space and Time Scale Variability and Interdependencies in Hydrological Processes. Cambridge University press, Cambridge.

Hubert, P., Bendjoudi, H., Schertzer, D., Lovejoy, S., 2001. Multifractal Taming of Extreme Hydrometeorological Events 2001.

Hurst, H.E., 1951. Long-term storage capacity of reservoirs. Trans. Am. Society Civil Eng. 116, 770–808.

Kumar, P., Foufoula-Georgiou, E., 1993. A new look at rainfall fluctuations and scaling properties of spatial rainfall. J. Appl. Meteorol. 32, 2.

Labat, D., Mangin, A., Ababou, R., 2002. Rainfoll-runoff relations for karstic springs: multifractal analyses. J. Hydrol. 256, 176–195.

Ladoy, P., Schmitt, F., Schertzer, D., Lovejoy, S., 1993. Variabilité temporelle des observations pluviométriques à Nimes. Comptes Rendues Acad. des Sci. 317 (II), 775–782.

Laferrière, A., Gaonac'h, H., 1999. Multifractal properties of visible reflectance fields from basaltic volcanoes. J. Geophys. Res. 104, 5115–5126.

Larnder, C., Observer problems in multifractals: The example of rain, MSc. thesis, McGill, Montreal, 1995.

Lavallée, D., Lovejoy, S., Schertzer, D., Ladoy, P., 1993. Nonlinear variability and landscape topography: analysis and simulation. In: De Cola, L., Lam, N. (Eds.), Fractals In Geography. Prentice-Hall, Englewood, NJ, pp. 171–205.

Levy-Véhel, J., Daoudi, K., Lutton, E., 1995. Fractals 2, 1.

Lewis, G., Austin, P.H., Szczodrak, M., 2004. Spatial statistics of marine boundary layer clouds, J. Geophys. Res. 109, D04104.

Lilley, M., Lidar measurements of passive scalars and the 23/9 dimensional model of atmospheric dynamics, MSc. thesis, McGill, Montreal, 2003.

Lilley, M., Lovejoy, S., Strawbridge, K., Schertzer, D., 2004. 23/9 dimensional anisotropic scaling of passive admixtures using lidar aerosol data. Phys. Rev. E 70 (036307-1-7).

Lilley, M., Lovejoy, S., Desaulniers-Soucy, N., Schertzer, D., in press. Multifractal large number of drops limit in Rain, J. Hydrol.

Lovejoy, S., Analysis of rain areas in terms of fractals, in 20th conference on radar meteorology, pp. 476–484, American Meteorological Society, Boston, Ma, 1981.

Lovejoy, S., 1982. Area perimeter relations for rain and cloud areas. Science 187, 1035–1037.

Lovejoy, S., Austin, G.L., 1979. The delineation of rain areas from visible and IR satellite data for GATE and mid-lattitudes. Atmos.-Ocean 17, 77–92.

Lovejoy, S., Schertzer, D., 1990. Multifractals, Universality classes and satellite and radar measurements of cloud and rain fields. J Geophys. Res. 95, 2021.

Lovejoy, S., Schertzer, D., 1991. Multifractal analysis techniques and the rain and clouds fields from 10^{-3} to 10^6 m. In: Schertzer, D., Lovejoy, S. (Eds.), Non-linear Variability in Geophysics: Scaling and Fractals. Kluwer, Dordecht, pp. 111–144.

Lovejoy, S., Schertzer, D., 1995a. How bright is the coast of Brittany?. In: Wilkinson, G. (Ed.), Fractals in Geoscience and Remote Sensing. Office for Official Publications of the European Communities, Luxembourg, pp. 102–151.

Lovejoy, S., Schertzer, D., 1995b. Multifractals and Rain. In: Kunzewicz, Z.W. (Ed.), New Uncertainty Conceps in Hydrology and Water Ressources. Cambridge University Press, Cambridge, pp. 62–103.

Lovejoy, S., Schertzer, D., Ladoy, P., 1986. Fractal characterisation of inhomogeneous measuring networks. Nature 319, 43–44.

Lovejoy, S., Schertzer, D., Tsonis, A.A., 1987. Functional box-counting and multiple dimensions in rain. Science 235, 1036–1038.

Lovejoy, S., Schertzer, D., Silas, P., Tessier, Y., Lavallée, D., 1993. The unified scaling model of atmospheric dynamics and systematic analysis in cloud radiances. Ann. Geophys. 11, 119–127.

Lovejoy, S., Duncan, M., Schertzer, D., 1996. The scalar multifractal radar observer's problem. J. Geophys. Res. 31D, 26,479–26,492.

Lovejoy, S., Schertzer, D., Stanway, J.D., 2001. Direct Evidence of planetary scale atmospheric cascade dynamics. Phys. Rev. Lett. 86 (22), 5200–5203.

Lovejoy, S., Lilley, M., Desaulniers-Soucy, N., Schertzer, D., 2003. Large particle number limit in Rain. Phys. Rev. E 68, 025301.

Lovejoy, S., Schertzer, D., Tuck, A.F., 2004. Fractal aircraft trajectories and nonclassical turbulent exponents. Phys. Rev. E 70 (036306-1-5).

Mandelbrot, B.B., 1974. Intermittent turbulence in self-similar cascades: Divergence of high moments and dimension of the carrier. J. Fluid Mechanics 62, 331–350.

Mandelbrot, B.B., Van Ness, J.W., 1968. Fractional Brownian motions, fractional noises and applications. SIAM Rev. 10, 422–450.

Marsan, D., Schertzer, D., Lovejoy, S., 1996. Causal space–time multifractal processes: predictability and forecasting of rain fields. J. Geophy. Res. 31D, 26,333–26,346.

Mazzarella, A., 1999. Multifractal dynamic rainfall processes in Italy. Theor. Appl. Climatol. 63, 73–78.

Menabde, M., Harris, D., Seed, A., Austin, G., Stow, D., 1997. Multiscaling properties of rainfall and bounded random cascades. Water Resources Res. 33 (12), 2823–2830.

Meneveau, C., Sreenivasan, K.R., 1987a. In: Van, M.-D. (Ed.), The physics of chaos and systems far from equilibrium.

Meneveau, C., Sreenivasan, K.R., 1987b. Simple multifractal cascade model for fully develop turbulence. Phys. Rev. Lett. 59 (13), 1424–1427.

Naud, C., Schertzer, D., Lovejoy, S., 1996. Fractional Integration and radiative transfer in multifractal atmospheres. In: Woyczynski, W., Molchansov, S. (Eds.), Stochastic Models in Geosystems. Springer-Verlag, New York, pp. 239–267.

Novikov, E.A., 1970. Intermittency and scale similarity of the structure of turbuoent flow. Prikl. Math. Mekh. 35, 266–277.

Olsson, J., 1995. Limits and Characteristics of the multifractal behavior of a high-resolution rainfall time series. Non-linear Process. Geophys. 2, 23–29.

Olsson, J., Niemczynowicz, J., Berndtsson, R., 1993. Fractal analysis of high resolution rainfall time series. J. Geophys. Res. 98, 23265–23274.

Over, T.M., Gupta, V.K., 1996a. A space–time theory of mesoscale rainfall using random cascades. J. Geophys. Res. 101, 26319–26331.

Over, T.M., Gupta, V.K., 1996b. Statistical analysis of mesoscale rainfall: Dependence of a random cascade generator on large scale forcing. J. Appl. Meteorol. 33, 1526–1542.

Pandey, G., Lovejoy, S., Schertzer, D., 1998. Multifractal analysis including extremes of daily river flow series for basis five to two million square kilometres, one day to 75 years. J. Hydrol. 208, 62–81.

Parisi, G., Frisch, U., 1985. A multifractal model of intermittency. In: Ghil, M., Benzi, R., Parisi, G. (Eds.), Turbulence and Predictability in Geophysical Fluid Dynamics and Climate Dynamics. Amsterdam, North Holland.

Pecknold, S., Lovejoy, S., Schertzer, D., Hooge, C., Malouin, J.F., 1993. The simulation of universal multifractals. In: Perdang, J.M., Lejeune, A. (Eds.), Cellular Automata: Prospects in Astronomy and Astrophysics. World Scientific, Singapore.

Richardson, L.F., Weather prediction by numerical process, Cambridge University Press republished by Dover, 1965, 1922.

Rosso, R., Burlando, P., 1990. Scale invariance in temporal and spatial rainfall. Ann. Geophys., special issue 1990;, 145.

Ruiz Chavarria, G., Baudet, C., Ciliberto, S., 1995. Europhys. Lett. 32, 413–419.

Sachs, D., Lovejoy, S., Schertzer, D., 2002. The multifractal scaling of cloud radiances from 1 m to 1 km, Fractals. 10, 253–265.

Salvadori, G., Schertzer, D., Lovejoy, S., 2001. Multifractal objective analysis and interpolation, Stoch. Environ. Resear. and Risk Analysis 15, 261–283.

Schertzer, D., Lovejoy, S., 1985a. The dimension and intermittency of atmospheric dynamics. In: Launder, B. (Ed.), Turbulent Shear Flow 4. Springer-Verlag, New York, pp. 7–33.

Schertzer, D., Lovejoy, S., 1985b. Generalised scale invariance in turbulent phenomena. Physico-Chem. Hydrodynamics J. 6, 623–635.

Schertzer, D., Lovejoy, S., 1987a. Physical modeling and analysis of rain and clouds by anisotropic scaling of multiplicative processes. J. Geophys. Res. 92, 9693–9714.

Schertzer, D., Lovejoy, S., 1987b. Singularités anisotrope, divergence des moments en turbulence. Annales de la Sosiété mathématique du Québec 11 (1), 139–181.

Schertzer, D., Lovejoy, S., 1992. Hard and soft multifractal processes. Phys. A 185, 187–194.

Schertzer, D., Lovejoy, S., 1997. Universal Multifractals do Exist!. J. Appl. Meteor. 36, 1296–1303.

Schertzer, D., Lovejoy, S., Schmitt, F., 1995. Schmitt, Structures in turbulence and multifractal universality. In: Meneguzzi, M., Pouquet, A., Sulem, P.L. (Eds.), Small-scale Structures in 3D and MHD Turbulence. Springer-Verlag, New York, pp. 137–144.

Schertzer, D., Lovejoy, S., Schmitt, F., Naud, C., Marsan, D., Chigirinskaya, Y., Marguerit, C. New developments and old questions in multifractal cloud modeling, satellite retrievals and anomalous absorption, in 7th Atmos. Rad. Meas. (ARM) meeting, edited by U. Dept. of Energy, pp. p327-335, San Antonio, 1997.

Schertzer, D., Lovejoy, S., Hubert, P. An Introduction to Stochastic Multifractal Fields, in Proceedings of the ISFMA Symposium on Environmental Science and Engineering with related Mathematical Problems, Series in Contemporary Applied Mathematics, High Education Press, Beijing (China). edited by A.E.a.W.L. editors, 2001.

Schmitt, F., Lavallée, D., Schertzer, D., Lovejoy, S., 1992. Empirical determination of universal multifractal exponents in turbulent velocity fields. Phys. Rev. Lett. 68, 305–308.

Schmitt, F., Schertzer, D., Lovejoy, S., Brunet, G., 1996. Universal multifractal structure of atmospheric temperature and velocity fields. Europhys. Lett. 34, 195–200.

Seed, A., 1989. Statistical Problems in Measuring Convective Rainfall. McGill University, Montréal (Québec), Canada.

She, Z.S., Levesque, E., 1994. Phys. Rev. Lett. 72, 336.

Stanway, J.D., Multifractal analysis of cloud radiances from 5000 to 1 km., MSc. thesis, McGill, Montreal, 2000.

Tessier, Y., Lovejoy, S., Schertzer, D., 1993. Universal Multifractals: theory and observations for rain and clouds. J. Appl. Meteorol. 32 (2), 223–250.

Tessier, Y., Lovejoy, S., Schertzer, D., 1994. The multifractal global raingage network: analysis and simulation. J. Appl. Meteorol. 32 (12), 1572–1586.

Tessier, Y., Lovejoy, S., Hubert, P., Schertzer, D., Pecknold, S., 1996. Multifractal analysis and modeling of rainfall and river flows and scaling, causal transfer functions. J. Geophy. Res. 31D, 26,427–26,440.

Turcotte, D.L., 1993. A scale-invariant approach to flood-frequency analysis. Stochastic Hydrol. Hydraul. 7, 33–40.

Veneziano, D., Bras, R.L., Niemann, J.D., 1996. Nonlinearity and self-similarity of rainfall in time and a stochastic model. J. Geophys. Res. 101, 26371–26392.

Waymire, E., Gupta, V.K., 1981. The mathematical structure of rainfall representations, 1, A review of stochastic rainfall models. Water Resour. Res. 17 (5), 1261–1272.

Wilson, J., Physically based stochastic modelling of rain and cloudfields, M. Sc. thesis, McGill University, Montréal (Québec), Canada, 1991.

Yano, J.J., McWilliams, J.C., Moncrieff, M.W., 1996. Fractality in idealized simulations of large-scale tropical cloud systems. Monthly Weather Rev. 124, 838–848.

Zawadzki, I., 1987. Fractal versus correlation structure in rain. J. Geophys. Res. 92, 469–472.

Zawadski, I., 1995. Is rain fractal?. In: Kundzewicz, A.W. (Ed.), New Uncertainty Concepts in Hydrology and Hydrological Modeling. Cambridge Univ. Press, Cambridge.